Desalination 643 (2027) 120952

Contents lists available at ScienceDirect

Desalination

journal homepage: www.elsevier.com/locate/desal

Defining practical membrane performance targets for hybrid semi-batch/batch reverse osmosis (HSBRO): From commercial limits to carbon-pricing economics

Hyowoog Gwak, Kiho Park *

Department of Chemical Engineering, Hanyang University, 222 Wangsimni-ro, Seongdong-gu, Seoul, 04763, Republic of Korea

HIGHLIGHTS

- Transport parameters were derived from commercial RO membrane specifications.
- Trade-offs between SEC and permeate quality were identified for RO membranes.
- Comprehensive performance was evaluated under diverse operating conditions.
- A practical permeability target for future membrane advancement was identified.
- The economic and carbon-related performance of HSBRO was quantified.

GRAPHICAL ABSTRACT



ARTICLE INFO

Keywords:
Hybrid semi-batch/batch reverse osmosis (HSBRO)
RO membrane
Permeability
Specific energy consumption (SEC)
Specific water cost (SWC)
Economic analysis

ABSTRACT

While hybrid semi-batch/batch reverse osmosis (HSBRO) offers compact, high-recovery desalination with exceptional energy efficiency, its full potential remains fundamentally constrained by intrinsic membrane properties. This study delineates the achievable performance limits of HSBRO by evaluating 26 commercial RO membranes through a comprehensive nonideal system model. By integrating specific energy consumption (SEC), permeate quality, specific water cost (SWC), and carbon-equivalent metrics, we assessed HSBRO performance, economics, and emissions associated with electricity supply across varying feed concentrations (1000–5000 ppm) and high recovery ratios (0.8 and 0.9). Across these cases, minimum SEC and SWC were 0.21 kWh/m^3 and \$0.36/m^3, respectively. Crucially, our analysis identifies a distinct threshold of diminishing returns: while increasing water permeability initially drives down SEC and SWC, the marginal benefits plateau beyond approximately 2.5×10^{-11} m/(s·Pa). This defines a practical target for future membrane advancement at 3000 ppm, subject to maintaining the required permeate quality. At the system level, strategic phase allocation proved highly synergistic; utilizing just 50% of the pure batch work-exchange vessel volume captured 99.8%–100.1% of the reference SEC reduction from semi-batch to pure-batch RO at a recovery of 0.9. Under PV power, increasing recovery from 0.8 to 0.9 remained economically favorable throughout the examined carbon price range of 0–0.3 USD/kgCO_2-eq; under diesel power, this advantage disappeared at approximately 0.18–0.20 USD/kgCO_2-eq, depending on membrane type. Ultimately, these findings bridge the gap between commercial

* Corresponding author.
E-mail address: kiho138@hanyang.ac.kr (K. Park).

https://doi.org/10.1016/j.desal.2026.120952
Received 27 July 2026; Received in revised form 29 September 2026; Accepted 15 October 2026
Available online 17 October 2026
0011-9164/© 2026 Elsevier B.V. All rights are reserved, including those for text and data mining, AI training, and similar technologies.

membrane capabilities and macro-level sustainability, providing a robust, target-driven framework for the design and operation of next-generation HSBRO systems.

Nomenclature

Roman and Greek symbols

ΔP_m	Pa, pressure drop inside the RO module
A	m/(s·Pa), water permeability
a	–, amortization factor
B	m/s, salt permeability
β	–, Size factor of HSBRO relative to that required for pure batch RO at the same recovery
C	mg/L, solute concentration
C_0	kg/m^3, feed concentration in parameter estimation model
$C_{advanced}$	\$/m^3, carbon tax equivalent costs at the advanced RO membrane permeability level
C_b	kg/m^3, bulk solution concentration
CC_{HPP}	\$, capital cost of a high-pressure feed pump
CC_{memb}	\$, capital cost of BWRO membrane modules
CC_{pre}	\$, water acquisition and pretreatment
CC_{recir}	\$, capital cost of a recirculation pump
$C_{current}$	\$/m^3, carbon tax equivalent costs at the current RO membrane permeability level
CC_{WEV}	\$, capital cost of work-exchange vessels
C_m	kg/m^3, membrane surface concentration
CP	–, concentration polarization correction factor
C_{perm}	kg/m^3, permeate concentration
C_{reten}	kg/m^3, outlet retentate concentration in parameter estimation model
D	m^2/s, diffusion coefficient
d_h	m, hydraulic diameter
E	kWh, energy consumption
e	\$/kWh, unit price of electricity
err_J	–, relative error between the guessed and updated water flux
f_m	–, friction factor in the membrane module
F_p	m^3/day, water production rate
H_f	m, feed channel height
i	–, ionization number
ir	yr^{-1}, annual interest rate
J_s	kg/(m^2·s), salt flux
J_w	m^3/(m^2·s), average water flux
k	m/s, mass-transfer coefficient
L	m, membrane module length
Lf	–, load factor
n	yr, plant lifetime
N_{RO}	–, the number of RO modules
N_{WEV}	–, the number of work-exchange vessels
OC_{chem}	\$/yr, operational cost of chemical treatment
OC_{elec}	\$/yr, operational cost of electricity
OC_{insure}	\$/yr, operational cost of insurance
OC_{labor}	\$/yr, operational cost of labor
$OC_{replace}$	\$/yr, operational cost of membrane replacement
P	Pa, pressure
$Price_{carbon}$	\$/kgCO_2-eq, carbon price
Q_{feed}	m^3/s (m^3/day), feed flow rate
$Q_{m,in}$	m^3/s, module inlet flow rate
$Q_{m,out}$	m^3/s, module outlet flow rate
Q_{recir}	m^3/s, recirculation flow rate
Q_{reten}	m^3/s, outlet retentate flow rate in parameter estimation model
R	Pa·m^3/(K·mol), gas constant
r	–, total recovery
r_b	–, batch pressurization phase recovery of HSBRO
R_s	–, salt rejection
r_{test}	–, recovery of the RO membrane test condition
Sc	–, Schmidt number
SEC_{HSBRO}	kWh/m^3, SEC of the HSBRO system
Sh	–, Sherwood number
T	K, temperature
TAC	\$/yr, total annual cost
$TACC$	\$/yr, total annualized capital cost
t_{bp}	s, duration of the batch pressurization phase
t_{br}	s, duration of the purge-and-refill phase
TCC	\$, total capital cost
TOC	\$/yr, total operating cost
t_{sb}	s, duration of the semi-batch phase

(*continued on next column*)

(*continued*)

V_{b0}	m^3, feed volumes introduced during the batch pressurization phase of HSBRO
V_m	m^3, volume inside the RO module
$V_{pipe,pg}$	m^3, pipe volume of the purge region
V_{sb0}	m^3, feed volumes introduced during the semi-batch phase of HSBRO
W	m, membrane width
z	m, axial position along the membrane module
α	–, recirculation flow ratio
η	– (%), pump efficiency
λ	–, longitudinal dispersion factor in the RO module
μ	Pa·s, viscosity
ν	m/s, cross-flow linear velocity within the RO module
π	Pa, osmotic pressure
ρ	kg/m^3, solution density
ω	–, relaxation factor

Subscript

b (or bp)	batch (pressurization phase)
Bat	battery
br	purge-and-refill phase (brine)
in	inlet
Inv	inverter
m	membrane
out	outlet
recir	recirculation
sb	semi-batch (phase)
WEV	work-exchange vessel

Abbreviations

BWRO	brackish water reverse osmosis
CAPEX	capital expenditure
CCRO	closed-circuit reverse osmosis
EU ETS	European union emissions trading system
HSBRO	hybrid semi-batch/batch reverse osmosis
LDH	layered double hydroxide
MLD	minimal liquid discharge
ODE	ordinary differential equation
OPEX	operational expenditure
PA	polyamide
PEG	polyethylene glycol
PV	photovoltaic
RO	reverse osmosis
SCE	specific carbon emission
SEC	specific energy consumption
SEF	specific carbon emission factor
SOTA	state-of-the-art
SWC	specific water cost
SWRO	seawater reverse osmosis
TAC	total annual cost
TACC	total annualized capital cost
TDS	total dissolved solids
TFC	thin-film composite
TOC	total operating cost
WHO	world health organization
WT	wind turbine
ZIF	zeolitic imidazolate framework
ZLD	zero liquid discharge

1. Introduction

Water scarcity driven by climate change and population growth has made sustainable desalination essential for global water security [1–5].

Reverse osmosis (RO) has established market dominance over thermal desalination technologies—such as multistage flash and multi-effect distillation—due to its vastly superior energy efficiency and cost-effectiveness. Standard seawater RO (SWRO) and brackish water RO (BWRO) typically operate at specific energy consumptions (SEC) of 2.5–4.0 kWh/m^3 and 0.5–2.5 kWh/m^3 with specific water costs (SWC) below \$0.7/m^3, compared to thermal processes requiring 5.5–27 kWh/m^3 and 0.7–1.5 USD/m^3 [6–10].

Despite its dominance, conventional continuous RO remains thermodynamically inefficient because it maintains a high feed pressure throughout the membrane flow path to sustain permeation [11,12]. This requirement arises from the increase in salt concentration and osmotic pressure on the feed side as permeate is produced, while sufficient hydraulic pressure must be applied to overcome the osmotic pressure difference across the membrane [11]. In the reversible limit, the applied hydraulic pressure approaches the osmotic pressure difference and all other losses vanish, so separation occurs without entropy generation and requires the minimum work [12,13]. In conventional continuous RO operated at a constant feed pressure, excess driving force contributes to irreversible losses. Batch RO reduces these losses by gradually increasing pressure as the solution becomes more concentrated, allowing closer operation to the reversible limit while remaining subject to practical losses [11,12]. However, pure batch RO can face substantial physical constraints at elevated recoveries, including massive high-pressure vessel footprints, extended piping, increased salt retention, and higher frictional pressure drops [14]. On the other hand, pure semi-batch RO offers a more compact configuration, but the large concentration difference between incoming feed and recirculated concentrate increases entropy generation during mixing and limits its energy efficiency [12,14]. To overcome these challenges, hybrid semi-batch/batch RO (HSBRO) was introduced [14]. By synergistically merging semi-batch and batch operations, HSBRO achieves compact footprint requirements, high water recovery, and exceptional energy efficiency [14–16].

Crucially, the performance of an HSBRO system—centered primarily on its RO modules and work-exchange vessels—is heavily dictated not only by system architecture but also by the intrinsic transport properties of the RO membrane itself. While manufacturers offer diverse commercial RO membranes, each exhibits distinct trade-offs between water permeability and solute rejection [17–20]. Current literature lacks a systematic benchmarking of HSBRO across these commercially available membranes, leaving the achievable performance envelope unclear. More importantly, as membrane synthesis advances, a critical question remains unanswered: *At what point do further increases in permeability yield diminishing returns in energy and cost for batch-type RO processes?* Establishing practical membrane advancement targets is therefore essential to guide future membrane material design.

Furthermore, the implementation potential of next-generation HSBRO systems must be evaluated in the context of the current emphasis on reducing carbon emissions from water infrastructure [21,22]. The energy savings enabled by HSBRO directly translate into reduced specific carbon emissions (SCE). Under emerging carbon pricing frameworks, these emissions internalize as concrete operating costs. Consequently, an adequate evaluation framework for HSBRO must transcend conventional SEC and SWC metrics to encapsulate carbon-pricing economics across variable grid carbon intensities.

To address these gaps, this study presents an integrated techno-economic and carbon emissions assessment of HSBRO by benchmarking 26 commercial RO membranes using a validated, nonideal process model. Transport parameters derived from manufacturer specifications were incorporated to establish realistic performance boundaries under varying feed concentrations (1000–5000 ppm) and high recovery ratios (0.8 and 0.9). We systematically quantify SEC, permeate quality, SWC, and SCE to: (1) delineate the achievable performance limits of HSBRO with existing commercial membranes; (2) identify the threshold of diminishing returns to define practical water permeability targets for future membrane development; (3) evaluate strategic phase allocation parameters; and (4) assess the economic resilience of HSBRO under various carbon taxation scenarios.

2. Methodology

2.1. Working principle of the HSBRO process

As illustrated in Fig. 1, the HSBRO system comprises a high-pressure feed pump, a piston-equipped work-exchange vessel, an RO membrane module, and a recirculation loop. Similar to conventional RO, HSBRO fundamentally operates by utilizing hydraulic pressure to overcome osmotic pressure for solute rejection and permeate generation. The HSBRO system combines semi-batch and batch operation in a hybrid configuration and is characterized by a cyclic sequence consisting of three distinct phases: semi-batch (Step 1), batch pressurization (Step 2), and purge-and-refill (Step 3). Permeate is produced during the first two phases, while the third phase removes accumulated brine and refills the system with fresh feed in preparation for the next cycle. Steps 1–3 constitute one complete HSBRO cycle, and this sequence is repeated during operation [14,15].

The cycle begins with the semi-batch phase, during which raw feed is continuously introduced into the system. The feed first enters the work-exchange vessel, where it mixes with the internal solution before reaching the RO membrane module. The primary advantage of HSBRO is that the work-exchange vessel effectively acts as a hydraulic buffer, mitigating the rapid concentration buildup that typically occurs in conventional semi-batch RO. During this phase, permeate is continuously extracted, while the retentate is recirculated and blended with the incoming feed. This operation is maintained until the salinity within the system reaches a predefined threshold (usually the level of internal concentration).

Subsequently, the system switches to the second phase, that is, the batch phase. The feed enters the work-exchange vessel to physically pressurize the free-piston. Permeate is produced as the feed pushes the free-piston forward, displacing the internal solution of the vessel across the RO membrane module. The concentrate that does not permeate the RO membrane is recirculated with the internal solution of the vessel and returned to the RO membrane module. This batch phase continues until the piston reaches the opposite end of the vessel.

Finally, the purge-and-refill phase resets the system. The highly concentrated brine accumulated within the RO membrane module and piping network is rapidly flushed out, while the vessel is concurrently refilled with fresh feed. The repetition of these three phases enables the HSBRO system to achieve high overall recovery by extending the operating time through the semi-batch and batch phases.

2.2. Membrane properties

Since the performance of an RO process is mainly affected by the intrinsic properties of the RO membrane, these properties must be rigorously quantified to analyze HSBRO performance. Table 1 summarizes the specifications of the commercial 8-in. BWRO membranes used in the simulation.

The specification data for the 26 commercial BWRO membranes were collected from eight global manufacturers: Aquaporin Inside®, DuPont FilmTec™, Nitto Hydranautics, LG Chem, Toray, CSM, SUEZ, and LANXESS. An 8-in. spiral-wound module was used as the reference model for all targeted membranes. The geometric properties such as the length, active area, and channel height of the RO membrane are key factors that determine the retention volume inside the RO membrane module. Owing to the cyclic operation of HSBRO, this volume affects the batch recovery ratio [14]. The higher salt rejection values reported in Table 1 indicate that the dense pore structure of the membrane effectively blocks contaminants, ensuring high permeate quality. However, this dense structure increases resistance to water molecule transport,

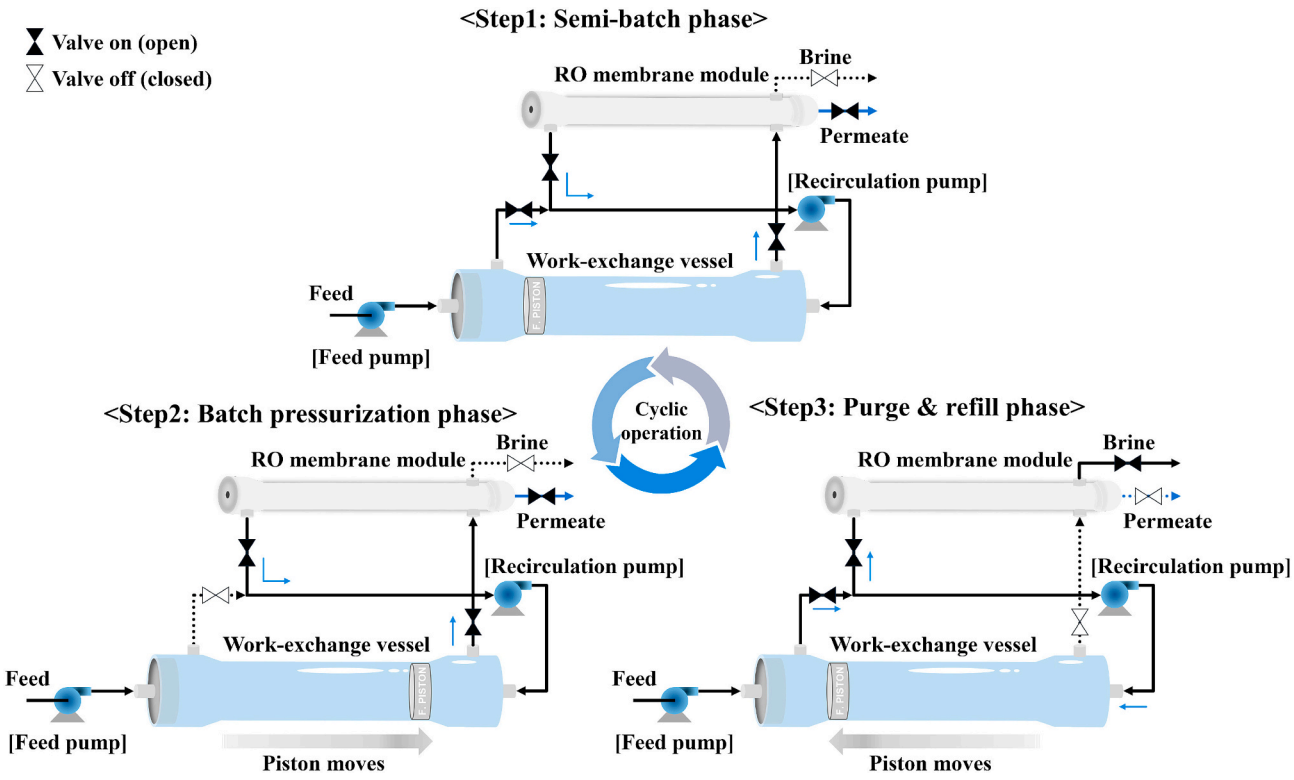


Fig. 1. Schematic illustration of the three phases of an HSBRO cycle: semi-batch (Step 1), batch pressurization (Step 2), and purge-and-refill (Step 3). Solid lines indicate active flow paths, whereas dotted lines indicate paths with no flow during the corresponding phase. Filled black and unfilled valve symbols denote open and closed valves, respectively. Small blue arrows indicate fluid flow direction, and large gray arrows beneath the work-exchange vessel indicate piston movement. The central curved arrows represent the repeated sequence of the three phases.

Table 1
Specifications of the 26 commercial 8-in. BWRO membranes used in the process simulations.

Membrane No.	Manufacturer	Model name	Length (m)	Active area (m^2)	Membrane width (m)	Hydraulic diameter (mm)	Salt rejection (%)
1	Aquaporin Inside®	CLEAR Eco 8040–440	1.0155	40.2	39.58641	0.3556	99
2		CLEAR Classic HR 8040–440	1.0155	40.2	39.58641	0.3556	99.8
3	DuPont FilmTec™	BW30HR-440	1.02	40.87732	40.0758	0.3556	99.7
4		BW30HRLE-440	1.02	40.87732	40.0758	0.3556	99.3
5		XLE-440	1.02	40.87732	40.0758	0.3556	98.31
6		Eco Pro-440	1.02	40.87732	40.0758	0.3556	99.7
7		BW30–400	1.02	37.1612	36.43255	0.3556	99.5
8	Nitto	CPA7-LD	1.02	37.1612	36.43255	0.4318	99.8
9	Hydranautics	CPA7-MAX	1.02	40.87732	40.0758	0.4318	99.8
10		ESPA2-LD-MAX	1.02	40.87732	40.0758	0.4318	99.6
11		ESPA4-MAX	1.02	40.87732	40.0758	0.4318	99.2
12	LG Chem	LG BW 440 R G2	1.02	40.87732	40.0758	0.3556	99.78
13		LG BW 440 ES	1.02	40.87732	40.0758	0.3556	99.6
14		LG BW 440 UES	1.02	40.87732	40.0758	0.3556	99
15	Toray	TM720D-440	1.02	40.87732	40.0758	0.3556	99.8
16		TMG20D-440	1.02	40.87732	40.0758	0.3556	99.7
17		TMH20A-440C	1.02	40.87732	40.0758	0.3556	99.3
18	CSM	RE8040-BE440	1.02	40.87732	40.0758	0.3556	99.7
19		RE8040-BLF440	1.02	40.87732	40.0758	0.3556	99.2
20		RE8040-BLN440	1.02	40.87732	40.0758	0.3556	99.2
21		RE8040-BLR440	1.02	40.87732	40.0758	0.3556	99.6
22	SUEZ	AK-440	1.02	40.87732	40.0758	0.3556	99.5
23		AG-440	1.02	40.87732	40.0758	0.3556	99.8
24	LANXESS	RO B440 HR	1.02	40.87732	40.0758	0.3556	99.7
25		RO B440 HF	1.02	40.87732	40.0758	0.3556	99.5
26		RO B440 LE	1.02	40.87732	40.0758	0.3556	99.5

thereby reducing the permeate flux under the same operating pressure. Consequently, additional energy consumption may be required to maintain the same permeate flux [17,23].

2.3. Parameter estimation and algorithm

In this study, mass transport across the RO membrane was analyzed using the solution–diffusion model. The average water flux (J_w) and salt

flux (J_s) are defined as follows [17,24–28]:

$$J_w = A(\Delta P - \Delta\pi), \tag{1}$$

$$J_s = B\left(C_m - C_{perm}\right), \tag{2}$$

where A and B represent the water permeability and salt permeability, respectively, ΔP is the applied pressure, $\Delta\pi$ is the osmotic pressure difference between the feed solution and the permeate, and C_m and C_{perm} are the membrane surface concentration and permeate concentration, respectively. In this model, the osmotic pressure contribution from the permeate side is neglected, and only the osmotic pressure caused by the membrane surface concentration is considered. The osmotic pressure (π) was calculated using the van't Hoff eq. [16]:

$$\pi = iCRT \tag{3}$$

where i is the ionization number, C is the concentration, R is the gas constant, and T is the temperature. During practical operation, concentration polarization occurs as solutes accumulate on the RO membrane surface. Therefore, the membrane surface concentration becomes higher than the bulk concentration, which can be expressed using the film theory equation as follows [29]:

$$C_m = C_b exp\left(\frac{J_w}{k}\right), \tag{4}$$

where C_b is the bulk solution concentration, and k is the mass-transfer coefficient. To accurately simulate the concentration polarization behavior, additional factors reflecting the fluid mechanics characteristics of the system were derived using Eqs. (5)–(8) [30,31]:

$$Re = \frac{\rho\nu d_h}{\mu}, \tag{5}$$

$$Sc = \frac{\mu}{\rho D}, \tag{6}$$

$$Sh = 0.2Re^{0.57}Sc^{0.4}, \tag{7}$$

$$k = \frac{Sh{\cdot}D}{d_h}, \tag{8}$$

where ρ and μ represent the solution density and viscosity, respectively; d_h is the hydraulic diameter, which is equal to half the feed channel height; D is the diffusion coefficient; ν is the cross-flow linear velocity within the RO module; Sc is the Schmidt number; and Sh is the Sherwood number. The parameters μ (Pa·s), ρ (kg/m^3), and D (m^2/s) depend on the solute concentration C (mg/L) and T (K) and are calculated as follows [30,32]:

$$\mu = \left(1.476\times10^{-3} + 2.482\times10^{-9}\times C + 9.329\times10^{-15}\times C^2\right) \times exp\left(-2.008\times10^{-2}\times(T-273.15)\right), \tag{9}$$

$$\rho = 997.05 + C\times10^{-3}, \tag{10}$$

$$D = 6.725\times10^{-6}\times exp\left(1.546\times10^{-7}\times C - \frac{2513}{T}\right). \tag{11}$$

Based on Eqs. (9)–(11), Table 2 summarizes the properties used in the parameter estimation process at a feed concentration of 3000 ppm and a temperature of 25 °C.

Table 2
Solution properties at a feed concentration of 3000 ppm at 25 °C.

Name	Value (unit)
Molar weight of NaCl	58.44 (g/mol)
Density (ρ)	1.00×10^3 (kg/m^3)
Viscosity (μ)	8.98×10^{-4} (Pa·s)
Diffusion coefficient (D)	1.47×10^{-9} (m^2/s)

The procedure for estimating the parameters A and B is illustrated as an algorithm flowchart in Fig. 2. This procedure is implemented using a nested calculation framework that combines an outer optimization loop for parameter estimation with a one-dimensional RO module simulation. The outer optimization loop provides trial values for A and B, while the RO simulation evaluates the corresponding membrane performance under the specified testing conditions. The estimated parameters are then updated by comparing the simulated performance with the target specification data.

In the RO simulation, the membrane module is discretized axially from the inlet to the outlet, and the local transport behavior is calculated point by point. At each axial position, the bulk concentration and osmotic pressure are first evaluated under the specified operating conditions. Since the local water flux (J_w), concentration polarization, membrane surface concentration, and membrane surface osmotic pressure are mutually coupled, J_w is obtained through an inner iterative calculation. The relative error between the guessed and updated water flux is defined by Eq. (12), and the guessed value is updated using the relaxation scheme in Eq. (13).

$$err_J = \frac{J_{w,guess} - J_w}{J_{w,guess}}, \tag{12}$$

$$J^{new}_{w,guess} = J_{w,guess} - \omega\left(J_{w,guess} - J_w\right), \tag{13}$$

where ω denotes the relaxation factor. Once the local flux converges, the converged J_w and the corresponding salt flux (J_s) are used to update the axial profiles of bulk concentration, cross-flow velocity, and pressure. The governing balance equations for the RO module calculation are expressed as:

$$\frac{dC}{dz} = \frac{C_b J_w - J_s}{\nu^*\left(0.5H_f\right)}, \tag{14}$$

$$\frac{d\nu}{dz} = -\frac{J_w}{0.5H_f}, \tag{15}$$

$$\frac{dP}{dz} = -\frac{f_m{}^*\mu^*\nu}{\left(0.5H_f\right)^2}, \tag{16}$$

where z is the axial position along the membrane module, H_f is the feed channel height (m), P is the local feed-side pressure (Pa), and f_m is the friction factor in the membrane module. Eq. (14) represents the salt mass balance within the feed channel, Eq. (15) accounts for the reduction in cross-flow velocity caused by permeation, and Eq. (16) describes the frictional pressure loss along the module. These equations are integrated along the module length, and the calculation proceeds to the next axial position until the outlet of the module is reached.

The geometric parameters of each RO membrane, including membrane area, module length, and feed channel height, were sourced from the membrane specification sheet. The operating conditions for parameter estimation were defined using the base test conditions summarized in Table 3. All parameter estimation calculations were performed at 25 °C. Under these test conditions, the target permeate flow rate and permeate concentration are defined as follows:

$$Q^{target}_{perm} = \nu_0 \times W \times 0.5H_f \times r_{test}, \tag{17}$$

$$C^{target}_{perm} = C_0 \times (1 - R_s), \tag{18}$$

where ν_0 is the inlet feed-channel velocity (m/s), W is the membrane width (m), r_{test} is the recovery of the test condition, C_0 is the feed concentration, and R_s is the salt rejection specified in the manufacturer specification data. For each trial set of A and B, the RO simulation was conducted to obtain the outlet retentate flow rate (Q_{reten}) and concentration (C_{reten}), which were calculated as follows:

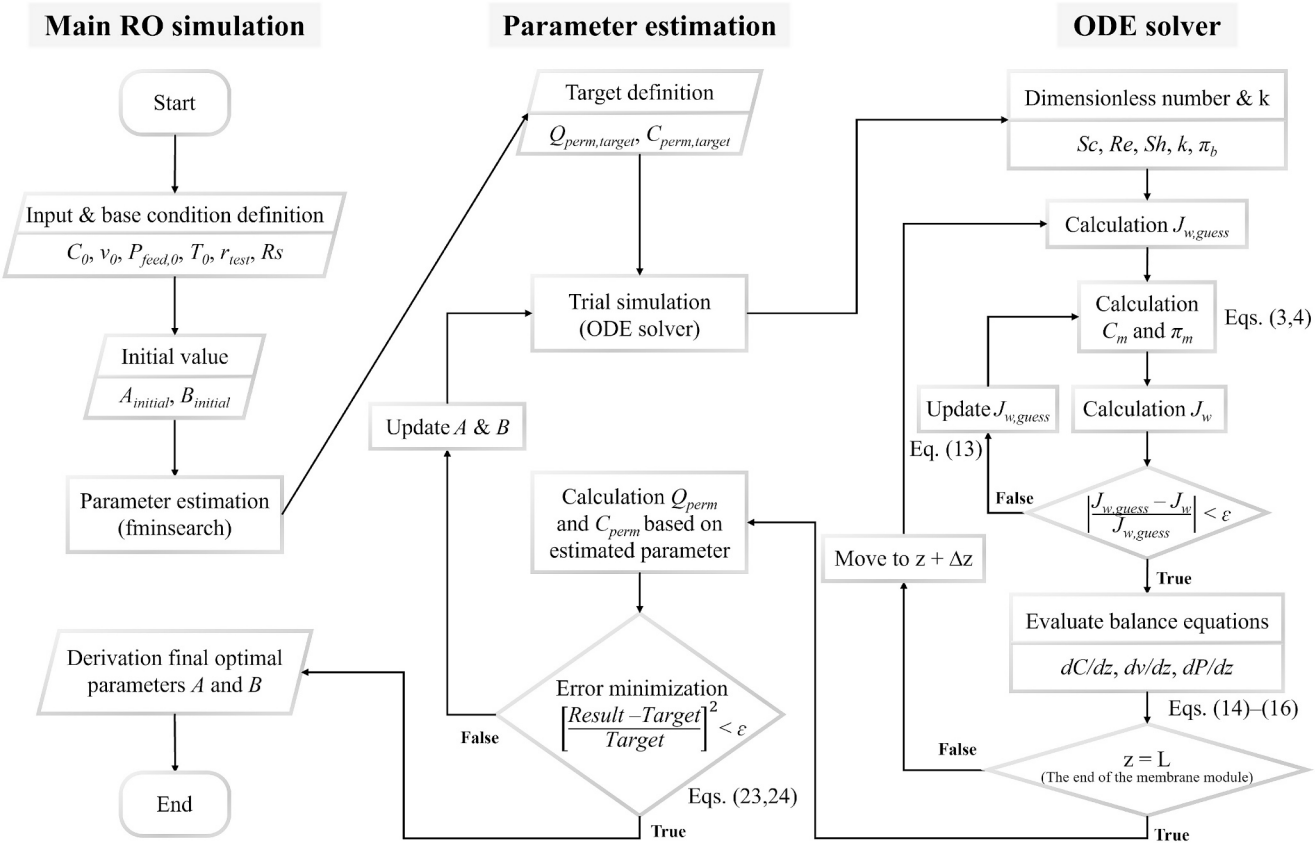


Fig. 2. Flowchart of the parameter estimation algorithm.

Table 3
Conditions used for parameter estimation and the obtained results (A and B).

No.	Manufacturer	Model name	Permeate flow rate (GPD)	Feed concentration (ppm)	Feed pressure (bar)	Recovery (%)	Water permeability (m/s/Pa)	Salt permeability (m/s)
1	Aquaporin Inside®	CLEAR Eco 8040–440	15,000	500	6.9	15	1.80×10^{-11}	1.19×10^{-7}
2		CLEAR Classic HR 8040–440	12,800	2000	15.5	15	1.04×10^{-11}	2.34×10^{-8}
3	DuPont	BW30HR-440	12,650	2000	15.5	15	1.01×10^{-11}	3.42×10^{-8}
4	FilmTec™	BW30HRLE-440	12,650	2000	10.3	15	1.65×10^{-11}	7.98×10^{-8}
5		XLE-440	12,389	2000	8.6	13.3	2.03×10^{-11}	1.92×10^{-7}
6		Eco Pro-440	12,650	2000	10.3	15	1.65×10^{-11}	3.42×10^{-8}
7		BW30–400	10,500	2000	15.5	15	9.20×10^{-12}	5.22×10^{-8}
8	Nitto	CPA7-LD	11,500	1500	15.5	15	9.71×10^{-12}	2.23×10^{-8}
9	Hydranautics	CPA7-MAX	12,600	1500	15.5	15	9.69×10^{-12}	2.23×10^{-8}
10		ESPA2-LD-MAX	12,000	1500	10.3	15	1.47×10^{-11}	4.25×10^{-8}
11		ESPA4-MAX	13,200	500	6.89	15	2.25×10^{-11}	9.31×10^{-8}
12	LG Chem	LG BW 440 R G2	12,650	2000	15.5	15	1.01×10^{-11}	2.51×10^{-8}
13		LG BW 440 ES	11,550	2000	10.3	15	1.50×10^{-11}	4.18×10^{-8}
14		LG BW 440 UES	12,650	2000	8.6	15	2.08×10^{-11}	1.14×10^{-7}
15	Toray	TM720D-440	12,100	2000	15.5	15	9.66×10^{-12}	2.19×10^{-8}
16		TMG20D-440	13,300	2000	10.3	15	1.74×10^{-11}	3.59×10^{-8}
17		TMH20A-440C	12,100	500	6.89	15	2.08×10^{-11}	7.65×10^{-8}
18	CSM	RE8040-BE440	11,500	2000	15.5	15	9.17×10^{-12}	3.12×10^{-8}
19		RE8040-BLF440	12,650	500	6.89	15	2.18×10^{-11}	9.13×10^{-8}
20		RE8040-BLN440	13,000	1500	10.3	15	1.60×10^{-11}	9.37×10^{-8}
21		RE8040-BLR440	9900	1500	10.3	15	1.21×10^{-11}	3.60×10^{-8}
22	SUEZ	AK-440	12,000	500	7.93	15	1.77×10^{-11}	5.42×10^{-8}
23		AG-440	12,000	2000	15.5	15	9.58×10^{-12}	2.17×10^{-8}
24	LANXESS	RO B440 HR	11,000	2000	15.5	15	8.77×10^{-12}	2.99×10^{-8}
25		RO B440 HF	11,600	2000	15.5	15	9.26×10^{-12}	5.25×10^{-8}
26		RO B440 LE	10,100	2000	10.3	15	1.31×10^{-11}	4.59×10^{-8}

$$Q_{reten} = W \times 0.5H_f \times \nu(L), \tag{19}$$

$$C_{reten} = C_b(L), \tag{20}$$

where L is the membrane module length, $\nu(L)$ is the local feed channel velocity at the module outlet, and $C_b(L)$ is the bulk concentration at the module outlet. Next, the corresponding permeate flow rate (Q_{perm}) and permeate concentration (C_{perm}) were obtained from the overall flow and salt mass balances:

$$Q_{perm} = \nu_0 \times W \times 0.5H_f - Q_{reten}, \tag{21}$$

$$C_{perm} = \frac{\nu_0 \times W \times 0.5H_f \times C_0 - Q_{reten}C_{reten}}{Q_{perm}}. \tag{22}$$

The simulated Q_{perm} and C_{perm} were subsequently compared with the corresponding target values. The relative error vector was first calculated to quantify the deviations of the simulated permeate flow rate and permeate concentration from their target values:

$$err = \left[\frac{Q_{perm} - Q_{perm}^{target}}{Q_{perm}^{target}}, \frac{C_{perm} - C_{perm}^{target}}{C_{perm}^{target}}\right]. \tag{23}$$

These two relative errors were combined into a single scalar fitting error using the sum of squared relative errors, as follows:

$$err_{sum} = \sum_i err_i^2, \tag{24}$$

where i denotes the relative error components corresponding to Q_{perm} and C_{perm}. This scalar error was minimized within the outer optimization loop to update the trial values of A and B. The estimation process was terminated when the relative deviations in both Q_{perm} and C_{perm} fell below the predefined tolerance. The parameter estimation procedure is summarized as follows:

1. Define the RO membrane specifications and input parameters, and initialize the trial values of A and B.
2. Calculate the target permeate flow rate and permeate concentration from the membrane specification data under the corresponding test condition.
3. Solve the RO module model from $z = 0$ to $z = L$ using the inlet boundary conditions [C_0, ν_0, $P_{feed,0}$, T_0].
4. At each axial position, calculate π_b, the dimensionless numbers, and the mass-transfer coefficient (k).
5. Set an initial guess for J_w, and calculate C_m and π_m using the concentration polarization relation and the van't Hoff eq.
6. Substitute π_m into the solution–diffusion equation to obtain an updated J_w.
7. Calculate the relative error between $J_{w,guess}$ and the updated J_w, and update $J_{w,guess}$ using the relaxation scheme.
8. Repeat steps 5–7 until the relative error in the local J_w, falls below the predefined tolerance of 10^{-8}, and then calculate the corresponding J_s.
9. Implement the converged J_w and J_s into the axial balance equations, and repeat the local calculation until the ordinary differential equation (ODE) solver reaches the module outlet.
10. Calculate Q_{reten}, C_{reten}, Q_{perm}, and C_{perm} from the outlet retentate values and the overall mass balance.
11. Compare the simulated Q_{perm} and C_{perm} against their target values, and calculate the relative error vector and err_{sum}.
12. Update parameters A and B via the outer optimization loop to minimize err_{sum}. If the error falls below the predefined tolerance of 10^{-15}, extract the final A and B values; otherwise, repeat steps 3–11.

Table 3 summarizes the base conditions used for parameter estimation and the obtained results for parameters A and B. No additional membrane experiments were conducted in this study. Model predictions obtained using estimated A and B values were benchmarked against DuPont WAVE for five representative DuPont membranes under reference and perturbed operating conditions. The comparison methodology and results are presented in Appendix G of the Supplementary Material.

2.4. HSBRO dynamic system modeling

The SEC, a key performance indicator for desalination processes, was calculated by summing the energy consumed during the three operation phases of a single HSBRO cycle as follows [14]:

$$SEC_{HSBRO} = \frac{E_{sb} + E_{bp} + E_{br}}{V_{sb0} + V_{b0}} = SEC_{sb} + SEC_{bp} + SEC_{br}, \tag{25}$$

where E_{sb}, E_{bp}, and E_{br} are the energy consumption of the semi-batch, batch, and purge-and-refill phases, respectively, and V_{sb0} and V_{b0} are the feed volumes introduced during the semi-batch and batch phases, respectively.

HSBRO exhibits dynamic behavior where the system concentration continuously changes throughout the operation. Therefore, modeling that accounts for nonidealities must be performed to estimate the practical energy consumption. The experimental validation of the HSBRO model was already conducted in the previous studies [15,16]. The nonideal correction factors considered in this study include salt retention, longitudinal concentration gradients, concentration polarization, pump efficiency, and frictional losses in the RO membrane, pipes, and inner walls [30]. The operating assumptions and the physical effects not explicitly modeled are specified in Section 2.7. The equations for calculating each energy term are as follows:

$$E_{sb} = \frac{1}{\eta_{feed}}\int_0^{t_{sb}} P_{feed}Q_{feed}dt + \frac{1}{\eta_{recir}}\int_0^{t_{sb}} P_{recir}Q_{recir}dt, \tag{26}$$

$$E_{bp} = \frac{1}{\eta_{feed}}\int_{t_{sb}}^{t_{sb}+t_{bp}} P_{feed}Q_{feed}dt + \frac{1}{\eta_{recir}}\int_{t_{sb}}^{t_{sb}+t_{bp}} P_{recir}Q_{recir}dt, \tag{27}$$

$$E_{br} = \frac{P_{feed,br}\left(V_m + V_{pipe,pg}\right)}{\eta_{feed}} + \frac{P_{recir,br}V_{b0}}{\eta_{recir}}, \tag{28}$$

$$V_0 = V_{b0} + V_m + V_{pipe,pg}, \tag{29}$$

where η is the pump efficiency; P is the required pump pressure; Q is the flow rate; t_{sb} and t_{bp} are the durations of the semi-batch and batch pressurization phases, respectively, as defined in Eqs. (45)–(46); V_m is the volume inside the RO module; and $V_{pipe,pg}$ is the pipe volume of the purge region. The numerical values of the parameters, including η and the volume, are summarized in Section 2.7. The feed flow rate (Q_{feed}), which is supplied by the feed pump, is kept constant during operation to maximize process efficiency. The recirculation flow rate (Q_{recir}) represents the non-permeated outlet flow from the RO module that is recirculated through the system, and it is defined as $Q_{recir} = \alpha Q_{feed}$ using the recirculation flow ratio α. To estimate the energy consumption, the required pump pressure at time is calculated as follows:

$$P_{feed}(t) = CP\left(\frac{\pi_{m,in}(t) + \pi_{m,out}(t)}{2}\right) + \frac{J_w}{A} + \frac{\Delta P_m}{2}, \tag{30}$$

$$P_{feed,br}(t) \cong \Delta P_m, \tag{31}$$

$$P_{recir}(t) \cong 2\Delta P_m, \tag{32}$$

$$P_{recir,br}(t) \cong \Delta P_m, \tag{33}$$

where CP is the concentration polarization correction factor, $\pi_{m,in}$ and $\pi_{m,out}$ are the osmotic pressures of the inlet and outlet streams within the RO module, respectively, and ΔP_m is the pressure drop inside the RO

module. During the purge-and-refill phase, osmotic pressure is neglected because permeation does not occur, and the required pressure is mainly associated with frictional losses in the RO module and pipes. To avoid undue complexity, the pressure drop in the pipes was assumed to be comparable to the frictional pressure loss in the RO module [31]. Accordingly, $P_{feed,br}$ and $P_{recir,br}$ were defined as ΔP_m. During the semi-batch and batch pressurization phases, P_{recir} represents the pressure required to overcome frictional losses in both the RO module and pipes and is therefore approximated as twice ΔP_m [14]. The osmotic pressure (π_m) in P_{feed} was evaluated from the internal concentration dynamics of the semi-batch and batch pressurization phases using the van't Hoff eq. The concentration balance equations for each phase are expressed as follows:

Semi-batch phase

$$\frac{dC_{m,in}}{dt} = \frac{Q_{feed}\left(\alpha\left(C_{m,out} - C_{m,in}\right) + \left(C_{feed} - C_{m,in}\right)\right)}{V_{b0} + V_{pipe,pg}}, \tag{34}$$

$$C_{0,sb} = C_{feed}\left(\frac{V_m + V_{pipe,pg} - Q_{feed}t_{sb}}{V_0} + \frac{\left(V_m + V_{pipe,pg}\right)\left(V_{b0} + Q_{feed}t_{sb}\right)}{V_0\left(V_m + V_{pipe,pg}\right)(1-\lambda)}\right), \tag{35}$$

$$C_{m,out} = C_{m,in} + \frac{2V_0\left(C_{0,sb} - C_{m,in}\right) + 2Q_{feed}C_{feed}t_{sb}}{V_m}, \tag{36}$$

Batch pressurization phase

$$\frac{dC_{m,in}}{dt} = \frac{\alpha Q_{feed}\left(C_{m,out} - C_{m,in}\right)}{V_{b0} + V_{pipe,pg} - Q_{feed}t_{bp}}, \tag{37}$$

$$C_{0,bp} = \frac{\left(V_{b0} + V_{pipe,pg}\right)C_{m,in}(t_{sb}) + 0.5V_m\left(C_{m,in}(t_{sb}) + C_{m,out}(t_{sb})\right)}{V_{b0} + V_m + V_{pipe,pg}}, \tag{38}$$

$$C_{m,out} = C_{m,in} + \frac{2V_0\left(C_{0,bp} - C_{m,in}\right) + 2Q_{feed}C_{m,in}t_{bp}}{V_m}, \tag{39}$$

where $C_{m,in}$ and $C_{m,out}$ denote the bulk solution concentrations at the inlet and outlet of the RO module, respectively, and λ is the longitudinal dispersion factor in the RO module. $C_{0,sb}$ is the initial concentration used to start the concentration calculation in the semi-batch. $C_{0,bp}$ represents the initial concentration of the batch pressurization phase after completion of the semi-batch phase. In Eq. (38), $C_{m,in}(t_{sb})$ and $C_{m,out}(t_{sb})$ denote the RO module inlet and outlet concentrations at the end of the semi-batch phase. In this study, $C_{m,in}$ was obtained by integrating the dynamic mass balance for each phase with an ODE solver. Conversely, $C_{m,out}$ was calculated algebraically from the corresponding mass balance at each time step. In the semi-batch phase, the dynamic balance includes both the recirculation contribution and the incoming feed contribution. In the batch pressurization phase, the effective system volume decreases with time as pressurization proceeds. The calculated C_m values were then converted to π_m using the van't Hoff eq.

The pressure derivation expression in Eq. (30) can be broadly divided into an osmotic pressure term and a frictional resistance term. The *CP* for the osmotic pressure term is expressed as Eq. (40) based on the Sherwood analogy, and reflecting this nonideal behavior enables a more accurate and reliable HSBRO process simulation [30,33–35].

$$CP = \frac{\pi_m}{\pi_b} = exp\left(\frac{J_w}{k}\right). \tag{40}$$

ΔP_m can be expressed using the Hagen–Poiseuille equation as follows [30]:

$$\Delta P_m = \frac{f_m \mu \nu L}{(d_h)^2}, \tag{41}$$

where f_m is the friction factor derived from experimentally validated literature data [36].

During the semi-batch and batch pressurization phases, the cross-flow velocity (ν) in the RO module is obtained from the average of the module inlet and outlet velocities. Since the flow velocity varies along the module, this averaging approach represents ν without explicitly resolving local velocity variations. During the purge-and-refill phase, no permeate is produced; therefore, the flow rate remains unchanged between the module inlet and outlet, and a single velocity is used. Furthermore, the feed and recirculation flow rates are no longer related by the recirculation flow rate ratio used during the pressurization phases and are therefore determined separately. The feed flow purges the concentrated brine from the RO module, whereas the recirculation flow refills the work-exchange vessel with fresh feed solution and returns the free-piston to its initial position. The corresponding velocities are expressed as follows:

$$\nu = \frac{Q_{m,in} + Q_{m,out}}{2d_h W} = \frac{(\alpha+1)Q_{feed} + \alpha Q_{feed}}{2d_h W}, \tag{42}$$

$$\nu_{feed,br} = \frac{Q_{feed}}{d_h W}, \tag{43}$$

$$\nu_{recir,br} = \nu_{feed,br} \times \left(\frac{V_{b0}}{V_m + V_{pipe,pg}}\right). \tag{44}$$

The mass balance of the HSBRO system changes over time. Thus, the duration of each phase and the required pressure must be determined to estimate the total energy consumption. The duration of each phase can be obtained based on Q_{feed} and the feed volumes required in each phase while considering the pipe volume in the practical design model [14]:

$$t_{sb} = \frac{V_m + V_{pipe,pg}}{Q_{feed}}\left(\frac{r}{1-r} - \frac{r_b}{1-r_b}\right), \tag{45}$$

$$t_{bp} = \frac{V_m + V_{pipe,pg}}{Q_{feed}}\left(\frac{r_b}{1-r_b}\right). \tag{46}$$

The HSBRO process has been investigated experimentally at pilot scale [15,16]. Hosseinipour et al. used an Eco Pro-440 membrane included among the 26 membranes evaluated in this study and reported hydraulic SEC predictions within 3% of measurements under the tested conditions [15]. Full-scale (> 1000 m^3/day) validation of the HSBRO configuration remains future work.

2.5. Cost analysis model

To analyze the system economics reasonably, conventional RO cost models were employed in this study. The costs were calculated by considering the energy consumption and treatment capacity of the HSBRO system. This section introduces a model that estimates the total annual cost by calculating the capital expenditure (CAPEX) and operational expenditure (OPEX). CAPEX represents the initial investment required before operation, including the costs associated with equipment installation, pretreatment systems, pump facilities, RO membrane modules, and work-exchange vessels. OPEX includes the costs incurred during operation, including electricity, insurance, membrane replacement, chemical treatment, and labor costs. The plant lifespan was assumed to be 20 years. To account for practical operating schedules, the load factor was set to 0.9 [37–39].

(1) Capital cost

Water acquisition and pretreatment

$$CC_{pre} = 996^{*}Q_{feed}^{0.8}, \tag{47}$$

where Q_{feed} is the flow rate of the feed entering the RO module (m^3/day). Eq. (47) is generally applied to SWRO processes handling seawater. Since membrane fouling and performance degradation are driven by the

same principles in both SWRO and BWRO, the purpose of pretreatment remains consistent. Thus, although this study focused on BWRO, the basic pretreatment configuration was assumed to be identical to SWRO [28]. This approach ensures a more rigorous economic analysis [40]. Therefore, the pretreatment cost was estimated using Eq. (47) without modification.

High pressure pump [41–43]:

$$CC_{HPP} = 52^{*}Q_{HP}{}^{*}\Delta P_{HP}, \tag{48}$$

$$CC_{recir} = 52^{*}Q_{recir}{}^{*}\Delta P_{recir}. \tag{49}$$

The HSBRO system utilizes two pump types: a feed pump and a recirculation pump. Q_{HP} and Q_{recir} represent the flow rates supplied through the feed pump and the recirculation pump (m^3/h), while ΔP_{HP} and ΔP_{recir} denote the maximum pressures applied to the feed pump and the recirculation pump (bar), respectively.

BWRO membrane [39,44]:

$$CC_{memb} = 900^{*}N_{RO}, \tag{50}$$

where N_{RO} is the number of RO modules [44].

Work-exchange vessel [45,46]:

$$CC_{WEV} = 1,000^{*}\left(\frac{V_{b0}}{V_{b0,ref}}\right)^{0.6}, \tag{51}$$

where $V_{b0,ref}$ is the reference volume calculated at an overall recovery of 0.9 and a vessel volume ratio of 50% relative to pure batch RO at the same recovery. A reference vessel cost of $1000 was assumed using a vessel price reported in the literature as a proxy [39]. The cost-scaling exponent of 0.6 was adopted following the conventional six-tenths rule [45,46].

Total capital cost (TCC) is calculated multiplying the aggregate sum of these individual component costs by a practical investment factor [25].

$$TCC = 1.411^{*}\left(CC_{pre} + CC_{HPP} + CC_{recir} + CC_{memb} + CC_{WEV}\right). \tag{52}$$

The total annualized capital cost (*TACC*) was calculated using the amortization factor as follows:

$$a = \frac{ir(ir+1)^{n}}{(ir+1)^{n}-1}, \tag{53}$$

$$TACC = a^{*}TCC, \tag{54}$$

where ir is the annual interest rate (yr^{-1}), n is the plant lifetime (yr), and a is the amortization factor.

(2) Operational cost

Electricity:

$$OC_{elec} = SEC_{HSBRO}{}^{*}Q_{feed}{}^{*}e^{*}Lf^{*}365. \tag{55}$$

where SEC_{HSBRO} is the SEC of the HSBRO system (kWh/m^3), e is the unit price of electricity ($/kWh), and Lf is the load factor.

Insurance [47]:

$$OC_{insure} = 0.005^{*}TCC. \tag{56}$$

Membrane replacement [37]:

$$OC_{replace} = 0.1^{*}CC_{memb}. \tag{57}$$

Chemical treatment [39]:

$$OC_{chem} = 0.0225^{*}F_{p}{}^{*}Lf^{*}365, \tag{58}$$

where F_p is the water production rate (m^3/day).

Labor [48]:

$$OC_{labor} = 0.01^{*}F_{p}{}^{*}Lf^{*}365. \tag{59}$$

The total operating cost was calculated as follows:

$$TOC = OC_{elec} + OC_{insure} + OC_{replace} + OC_{chem} + OC_{labor}. \tag{60}$$

The total annual cost (*TAC*) and SWC are expressed as follows [39]:

$$TAC = TACC + TOC, \tag{61}$$

$$SWC = \frac{TAC}{F_{p}{}^{*}Lf^{*}365}. \tag{62}$$

2.6. Carbon emission and carbon tax equivalent cost analysis

To evaluate the environmental implications of energy use in HSBRO operation, SCE was estimated from the system SEC and the specific emission factor (SEF) for each electricity source and auxiliary power-system component. The SEF represents CO_2-equivalent emissions per unit of energy supplied, and Table 4 summarizes the values adopted in this study [49]. The assessment excludes emissions from desalination equipment manufacture and plant construction, membrane replacement, chemical supply, downstream brine treatment and disposal, and decommissioning. It therefore does not constitute a complete life-cycle assessment of the desalination system.

For the photovoltaic (PV) panel- and wind turbine (WT)-powered cases, inverters and batteries were included as auxiliary components to account for power conversion and storage during renewable-powered operation. In contrast, the diesel-powered case was assumed to directly supply electricity to the HSBRO system. Accordingly, no additional auxiliary components were included in the SCE calculation.

The SCE of the HSBRO system was calculated by multiplying the SEC by the corresponding SEF values listed in Table 4. For the PV-, WT- and diesel-powered cases, the SCE was estimated as follows [49]:

$$SCE_{PV} = SEC_{HSBRO} \times (SEF_{PV} + SEF_{Inv} + SEF_{Bat}), \tag{63}$$

$$SCE_{WT} = SEC_{HSBRO} \times (SEF_{WT} + SEF_{Inv} + SEF_{Bat}), \tag{64}$$

$$SCE_{Diesel} = SEC_{HSBRO} \times SEF_{Diesel}. \tag{65}$$

To quantify the economic implications of carbon emissions, the carbon tax equivalent cost was calculated by multiplying carbon price by the estimated SCE. In this study, the 2025 European union emissions trading system (EU ETS) average auction price of $0.08297/kg$CO_2$-eq was used as the base-case reference carbon price [50]. For the RO membrane advancement analysis, the avoided carbon tax equivalent cost was calculated relative to the current technology level of each membrane type:

$$C_{scenario,type} = SCE_{scenario,type} \times Price_{carbon}, \tag{66}$$

$$C_{avoided,type} = C_{current,type} - C_{advanced,type}, \tag{67}$$

where the subscript *scenario* denotes either the current or advanced membrane permeability level, $Price_{carbon}$ is the carbon price ($/kg$CO_2$-eq), and $C_{current}$ and $C_{advanced}$ are the carbon tax equivalent costs ($/$m^3$) at the current and advanced RO membrane permeability levels, respectively. This formulation enables the carbon emission and carbon

Table 4
SEFs used to calculate the SCE [49].

Components	SEF	Unit
PV panels	0.045	kgCO_2-eq/kWh
Wind turbines	0.011	kgCO_2-eq/kWh
Inverters	0.004	kgCO_2-eq/kWh
Batteries	0.028	kgCO_2-eq/kWh
Diesel fuel	0.888	kgCO_2-eq/kWh

cost benefits of RO membrane advancement to be evaluated based on the SEC reduction of the HSBRO system.

To evaluate the effect of carbon pricing on the economic performance of HSBRO, the carbon-adjusted SWC was calculated by adding the carbon tax equivalent cost to the original SWC. The carbon-adjusted SWC ($/m^3) is expressed as follows [51]:

$$SWC_{carbon} = SWC + SCE \times Price_{carbon}. \quad (68)$$

The same electricity price was applied to PV, WT, and diesel, and the investment and replacement costs of electricity supply equipment were not separately included. Consequently, for a given membrane and operating condition, differences in the carbon-adjusted SWC among the three scenarios arise solely from their emission factors and corresponding carbon tax equivalent costs. The comparison therefore isolates the influence of electricity supply emissions under common electricity cost assumptions.

Since high recovery increases water production from a specified feed volume, operating at a recovery ratio of 0.9 can reduce the SWC by distributing the system cost over a larger permeate volume. However, this economic benefit may be accompanied by an increase in SCE due to the increased energy requirement associated with high-recovery operation. Therefore, the economic advantage of a recovery of 0.9 should be evaluated by considering both its SWC reduction and the additional carbon cost associated with the increased SCE. The SWC advantage of a recovery of 0.9 over a recovery of 0.8 and the additional SCE associated with the former are defined as follows:

$$\Delta SWC = SWC_{0.8} - SWC_{0.9}, \quad (69)$$

$$\Delta SCE = SCE_{0.9} - SCE_{0.8}, \quad (70)$$

where the subscripts 0.8 and 0.9 denote recovery ratios of 0.8 and 0.9, respectively. ΔSWC represents the SWC reduction achieved by increasing the recovery from 0.8 to 0.9, and ΔSCE represents the additional SCE associated with the recovery ratio of 0.9. Using ΔSWC and ΔSCE, the net carbon-adjusted SWC (ΔSWC_{carbon}) advantage of a recovery of 0.9 was calculated by subtracting the additional carbon tax equivalent cost from the original SWC advantage:

$$\Delta SWC_{carbon} = \Delta SWC - \Delta SCE \times Price_{carbon} = SWC_{carbon,0.8} - SWC_{carbon,0.9}. \quad (71)$$

As the carbon price increases, the additional carbon cost associated with a recovery of 0.9 reduces its SWC advantage. To quantify the carbon price at which this advantage is completely offset, the break-even carbon price $Price_{carbon,BE}$ was introduced. This threshold corresponds to the carbon price where the SWC reduction achieved by a recovery of 0.9 becomes equal to its additional carbon tax equivalent cost. By setting $\Delta SWC_{carbon} = 0$, $Price_{carbon,BE}$ is obtained as follows:

$$Price_{carbon,BE} = \frac{\Delta SWC}{\Delta SCE}. \quad (72)$$

The value of $Price_{carbon,BE}$ represents the carbon price level at which the economic advantage of operating at a recovery ratio of 0.9 over 0.8 is fully offset by the additional carbon tax equivalent cost. When $Price_{carbon} < Price_{carbon,BE}$, a recovery ratio of 0.9 remains favorable in terms of the carbon-adjusted SWC. When $Price_{carbon} > Price_{carbon,BE}$, the additional carbon cost outweighs the SWC reduction benefit of the higher recovery ratio (0.9).

2.7. HSBRO process simulation conditions and variables

This section defines the model parameters and operating variables used for the HSBRO process simulation, cost analysis, and carbon assessment. The complete set of model inputs, operating conditions, and economic parameters is summarized in Table 5. The feed stream was modeled as an aqueous NaCl solution, and the ionization number of NaCl, i, was applied in the osmotic pressure calculation (Eq. (3)). The feed flow rate in the HSBRO simulation was fixed at 21.6 m^3/day. The feed concentration was varied within a typical brackish water range of 1000–5000 ppm, with 3000 ppm adopted as the base case condition for evaluating the 26 commercial RO membranes. The recirculation ratio was set to $\alpha = 3$ as the reference operating condition. The sensitivity analysis supporting this selection is presented in Appendix H of the Supplementary Material (Fig. S6 and Table S6). The module friction factor and recirculation pump efficiency were set to 20 and 0.5, respectively. In addition, sensitivity analyses were conducted to assess the effects of these parameters on the predicted SEC, with the analysis conditions and results presented in Appendix I of the Supplementary Material (Fig. S7). Fouling and scaling were assumed to be sufficiently controlled by pretreatment and antiscalant addition. Membrane compaction was not explicitly modeled, and the membrane permeability parameters were held constant during each simulation. All simulations were performed under steady feed conditions without temporal fluctuations in the feed concentration or feed temperature. Thermal effects within the HSBRO system were assumed to be negligible, and the process was modeled as isothermal without solving an energy balance.

The baseline target total recovery was set to 0.8, and the same simulation procedure was applied at a total recovery of 0.9 to evaluate certain performance indicators under high-recovery conditions. For each total recovery, the batch pressurization recovery (r_b) was determined such that the work-exchange vessel volume required for HSBRO was one-half of the vessel volume required for a full batch RO process at the same total recovery. Accordingly, the r_b values were 0.67 and 0.82 at total recoveries of 0.8 and 0.9, respectively. The volume of the RO module (V_m) was calculated by accounting for the active membrane volume and the dead volume inside the ports of the 8-in. RO module. The initial work-exchange vessel volume, corresponding to the batch-phase feed volume V_{b0}, was then determined from V_m, the pipe

Table 5
Model parameters and operating variables used for the HSBRO simulation, cost analysis, and carbon analysis.

Name	Value	Unit	Ref.
i	1.8648	–	[30]
ω	0.2	–	–
f_m	20	–	[14,36]
H_f	$= 2d_h$	m	[14]
V_{b0}	$= (V_m + V_{pipe,pg}) \times \frac{r_b}{1 - r_b}$	m^3	[14]
V_m	$= membrane\ area \times hydraulic\ diameter + 1.26 \times 10^{-3}$	m^3	[14]
$V_{pipe,pg}$	2.8458×10^{-4}	m^3	[14]
η_{feed}	70	%	[14]
η_{recir}	50	%	[14]
λ	0.08	–	[52]
α	3	–	[14]
Q_{feed}	21.6	m^3/day	[14]
r_b (at $r = 0.8$)	0.67	–	–
r_b (at $r = 0.9$)	0.82	–	–
t_{sb}	116–151 at $r = 0.8$; 262–341 at $r = 0.9$	s	–
t_{bp}	119–156 at $r = 0.8$; 269–350 at $r = 0.9$	s	–
t_{br}	59–77 at $r = 0.8$; 59–77 at $r = 0.9$	s	–
t_{all}	295–384 at $r = 0.8$; 590–768 at $r = 0.9$	s	–
N_{RO}	1	–	–
N_{WEV}	1	–	–
ir	0.06	yr^{-1}	[53]
n	20	yr	[39]
Lf	0.9	–	[54]
e	0.08	$/kWh	[39]
F_p	$= Q_{feed} \times r$	m^3/day	–
$Price_{carbon}$	0.08297 (base-case reference value)	$/ kg$CO_2$-eq	[50]
	0–0.3 (sensitivity range)	$/ kg$CO_2$-eq	–

volume of the purge region ($V_{pipe,pg}$), and the selected r_b. The durations of the semi-batch, batch pressurization, and purge-and-refill phases, denoted as t_{sb}, t_{bp} and t_{br}, respectively, were determined by the membrane geometry and recovery conditions, and are reported as ranges in Table 5. The permeate flow rate (F_p) was determined according to the total recovery ratio (r). The baseline BWRO simulations were subject to a maximum allowable pressure of 41 bar, and cases exceeding this limit were excluded from the baseline performance analysis. A separate assessment used a hypothetical pressure limit of 81 bar to examine operation at higher feed salinities, as described in Section 3.2.1.

3. Results and discussion

3.1. HSBRO performance evaluation using the commercial 8-in. RO membranes

Fig. 3 presents a comprehensive evaluation of the properties and HSBRO performance of the 26 commercial 8-in. BWRO membranes, including SEC, permeate quality, peak pressure, and SWC, under representative operating conditions. The distribution of A and B for the commercial 8-in. BWRO membranes is illustrated in Fig. 3a. This distribution demonstrates a characteristic trade-off between water permeability and water-solute selectivity in commercial BWRO membranes, as directly revealed by the fitted correlation curve in Fig. 3a. The fitted relation, $A = 3.46 \times 10^{-8} \times B^{0.46}$, indicates that the low SEC associated with high A tends to coincide with a deterioration in permeate quality resulting from the corresponding increase in B, and vice versa. Further details are provided in Appendix A of the Supplementary Material. This nonlinear correlation is consistent with the permeability–selectivity trade-off reported for polymeric desalination membranes, where enhanced water transport is generally accompanied by reduced salt rejection [23,55]. Within the solution–diffusion framework, this trade-off can be attributed to structural changes in the selective layer that facilitate water transport while also lowering the resistance to salt transport [23].

The HSBRO simulation results for each RO membrane are presented in Fig. 3b in terms of average permeate concentration, SEC, and peak pressure. The peak pressure for all RO membranes remained below

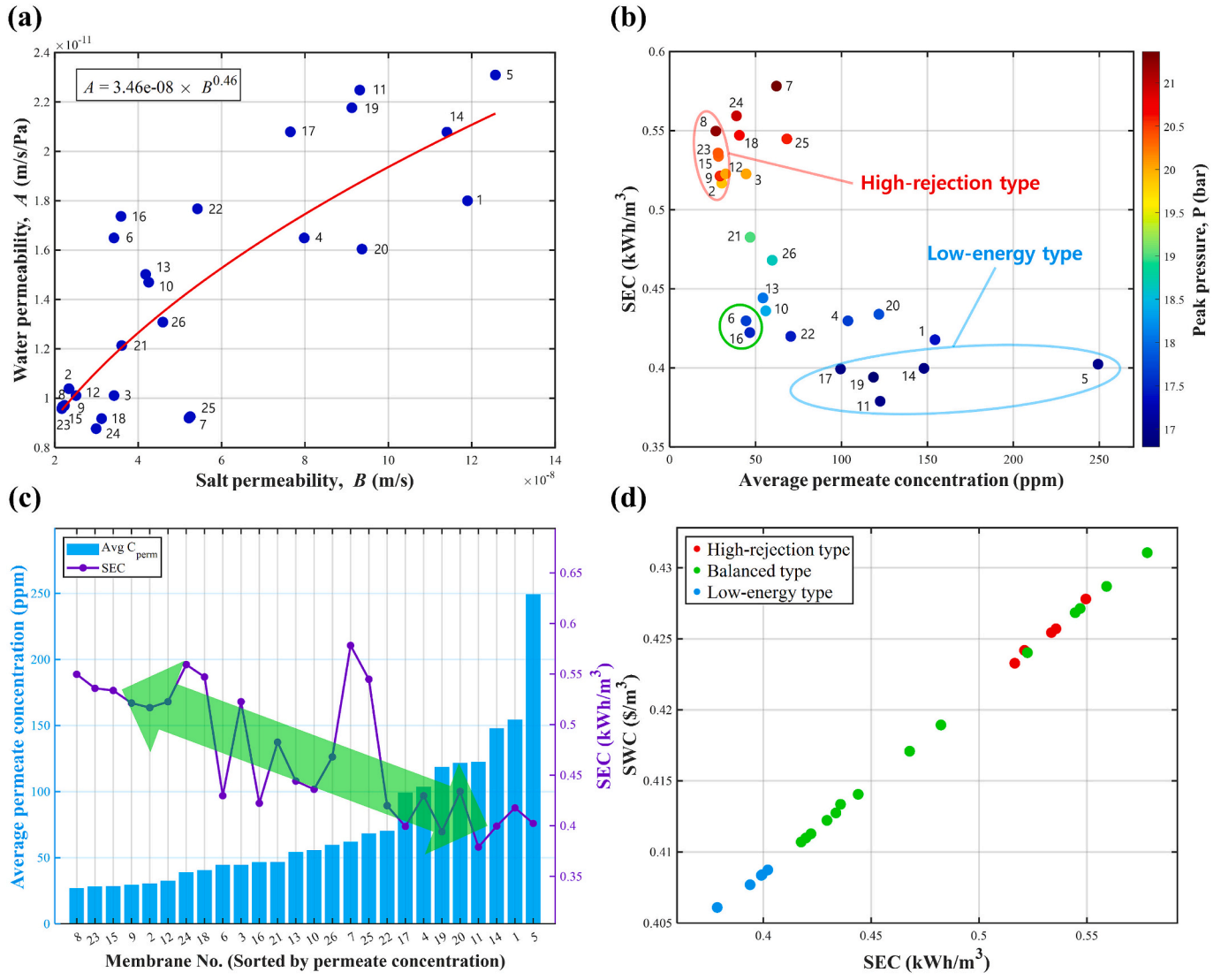


Fig. 3. Membrane properties and HSBRO performance analysis for the 26 commercial 8-in. BWRO membranes. (a) Distribution of the estimated A and B at 25 °C, along with the fitted power-law correlation. Each point represents an individual membrane, and the membrane numbers correspond to the identifiers listed in Table 1. (b) SEC–permeate quality relationship at a feed concentration of 3000 ppm and a total recovery of 0.8, with the colour scale denoting the corresponding peak pressure. (c) Individual membrane performance under the same operating conditions as in (b), arranged in ascending order of average permeate concentration. The bars indicate the average permeate concentration, and the line indicates the SEC. (d) Correlation between SEC and SWC under the same operating conditions, classified by membrane type.

22 bar within the allowable BWRO pressure limit (41 bar). As shown in the graph, an L-shaped Pareto front was formed, indicating a clear trade-off between permeate quality and energy efficiency. The point marked with a green circle in Fig. 3b indicates a condition that balances both energy consumption and permeate quality. Beyond this point, further reductions in permeate concentration cause a sharp increase in SEC while providing only marginal improvement in water quality. Therefore, membranes located near this point can be regarded as suitable candidates for satisfying the target permeate quality with limited associated energy penalty under the specified operating conditions.

After sorting the membranes in ascending order of average permeate concentration, their SEC values are compared in Fig. 3c. Although local fluctuations in SEC were observed due to differences in the intrinsic properties of the individual RO membranes, the overall trend indicates that SEC increases as the average permeate concentration decreases, as shown by the green arrow in Fig. 3c. Collectively, Fig. 3b and c illustrate the attainable trade-off between permeate quality and energy efficiency for the current commercial RO membrane technology.

The SEC–SWC relationship for the 26 commercial RO membranes applied to the HSBRO system is presented in Fig. 3d. At a recovery of 0.8 and a feed concentration of 3000 ppm, the SWC ranged from 0.406 to 0.431 USD/m^3, while the SEC varied from 0.379 to 0.578 kWh/m^3. Relative to their respective minimum values, membrane selection therefore produced a 52.6% variation in SEC but a 6.1% variation in SWC. The substantial variation in SEC does not translate proportionally into SWC because electricity cost represents only one component of the total water production cost.

The plausibility of HSBRO economics was further assessed by comparing the calculated SWC values of the HSBRO system with SWCs reported for other BWRO processes, as summarized in Table 6. Moreover, because pretreatment costs were not included in any of the reference studies, they were likewise excluded from the HSBRO calculations. The electricity price, feed concentration, and recovery were adjusted to the conditions adopted in each reference study, while the baseline HSBRO treatment capacity of 21.6 m^3/day was maintained. The lower HSBRO values in Table 6 compared to those presented in Fig. 3d are attributable primarily to the exclusion of pretreatment costs and the different electricity prices used in the comparative cases. Across the investigated conditions, the reported BWRO costs ranged from approximately 0.14 to 0.28 USD/m^3, whereas the corresponding HSBRO estimates ranged from 0.12 to 0.20 USD/m^3. The lower calculated HSBRO costs support the economic feasibility of the HSBRO system relative to previously reported BWRO processes under the investigated conditions. However, the reference systems operate at capacities of 3360–10,000 m^3/day, which are substantially greater than the baseline HSBRO capacity. Accordingly, large-scale implementation will require additional scale-up strategies, including parallel membrane modules, shared pumping infrastructure, and coordinated multi-train operation. The favorable economic performance of HSBRO despite its relatively small scale indicates that it can serve as an effective option for compact, decentralized desalination, particularly in onsite applications [14].

3.2. HSBRO performance evaluation under different operating conditions

3.2.1. Effects of feed concentration and recovery

Fig. 4 presents the simulation results illustrating how feed concentration and process recovery affect the SEC and average permeate concentration of the 26 RO membranes. At a recovery ratio of 0.9, conditions above a feed concentration of approximately 3540 ppm were excluded from the analysis because the required operating pressure exceeded the maximum allowable pressure of commercial BWRO membranes. The results at recovery ratios of 0.8 and 0.9 were obtained for an aqueous NaCl model solution under the assumption that scaling is adequately controlled, as specified in Section 2.7. For real brackish waters, mineral scaling may limit the achievable recovery before hydraulic or membrane pressure limits are reached. At a feed concentration of 3000 ppm, the SEC of the HSBRO process ranged from 0.38 to 0.58 kWh/m^3 at a recovery ratio of 0.8 (Fig. 4a) and from 0.46 to 0.66 kWh/m^3 at a recovery ratio of 0.9 (Fig. 4b). For comparison, other BWRO process has been reported to require 0.42–0.60 kWh/m^3 at a feed concentration of 2183–3231 ppm and a recovery ratio of 0.8, as well as 0.59–0.67 kWh/m^3 at 2900 ppm and a recovery ratio of 0.88 [12,58]. Detailed comparisons with literature data for other feed concentrations and RO configurations are provided in the Supplementary Material (Table S1) [12,58–62]. These results demonstrate that HSBRO offers an energy-efficient process configuration for brackish water desalination.

The SEC penalty associated with increasing recovery became more pronounced as the feed concentration increased. Based on the mean performance of the 26 RO membranes, increasing the recovery ratio from 0.8 to 0.9 raised the SEC by 9.4% at 1000 ppm but by 17.5% at 3000 ppm. Although the maximum module osmotic pressure approximately doubled at both concentrations, its effect on the SEC depended on its contribution to the total energy demand. At 1000 ppm, hydraulic losses and energy consumption during purge and refill constituted a substantial baseline demand, thereby limiting the increase in SEC. By contrast, at 3000 ppm, increasing the recovery ratio from 0.8 to 0.9 raised the maximum module osmotic pressure from 12.7 to 25.6 bar. Because osmotic pressure accounted for a larger proportion of the total energy demand under this condition, the recovery increase translated more directly into elevated SEC.

The corresponding permeate quality profiles are presented in Fig. 4c and d. At a feed concentration of 5000 ppm and a recovery ratio of 0.8, HSBRO produced permeate concentrations of 45–415 ppm, compared to the 470 ppm reported for CCRO under the same conditions [60]. At 3000 ppm and a recovery of 0.9, HSBRO yielded 36–330 ppm compared with the CCRO value of 360 ppm reported at the same feed concentration and recovery [60]. Other BWRO studies have reported permeate concentrations of 12–45 ppm at a feed concentration of 1000 ppm and 50–100 ppm at feed concentrations of 2500–5000 ppm [63,64]. Overall, the predicted HSBRO permeate concentrations overlapped with reported BWRO ranges and were generally comparable to or lower than the selected CCRO reference values, depending on membrane selection.

Within the baseline feed concentration range of 1000–5000 ppm and under pressure-feasible operating conditions, all commercial RO

Table 6
Comparison of reported SWCs for BWRO processes with the corresponding HSBRO estimates across matched electricity prices, feed concentrations, and recoveries, with pretreatment costs excluded for consistency and the baseline HSBRO treatment capacity maintained at 21.6 m^3/day.

e ($/kWh)	Feed concentration (ppm)	Recovery	Capacity (m^3/day)	SWC_{RO} from references ($/$m^3$)	SWC_{HSBRO} in this study ($/$m^3$)
0.08	3000	0.86	3360	0.22 [25]	0.16
	6000	0.83	3480	0.24 [25]	0.20
0.07	950	0.8	8389	0.22–0.25 [56]	0.12
	950	0.9	7456	0.19 [56]	0.12
0.067	1000	0.8	10,000	0.14 [57]	0.12
	3000			0.21 [57]	0.14
	5000			0.24 [57]	0.17
	7000			0.28 [57]	0.19

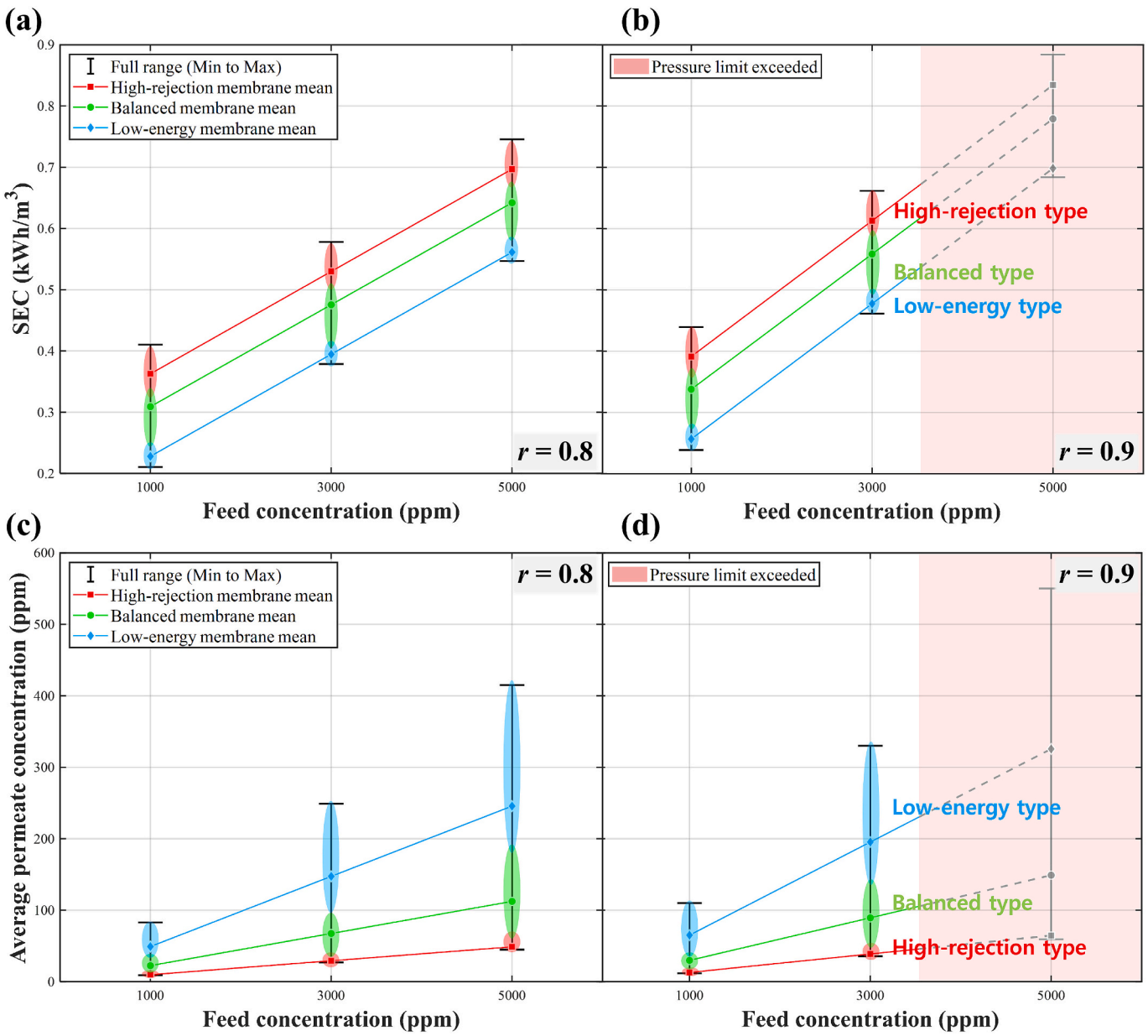


Fig. 4. HSBRO performance variation among 26 commercial 8-in. RO membranes at different feed concentrations and recovery ratios. SEC profiles at recovery ratios of (a) 0.8 and (b) 0.9. Average permeate concentrations at recovery ratios of (c) 0.8 and (d) 0.9. Feed concentrations of 1000, 3000, and 5000 ppm were considered. At a recovery ratio of 0.9, the required operating pressure exceeded the maximum allowable pressure of commercial BWRO membranes above approximately 3540 ppm. This region is indicated by light red shading and excluded from the analysis. The black error bars denote the full membrane performance range, and the colored markers indicate the mean values for the high-rejection, balanced, and low-energy membrane groups.

membranes applied to HSBRO produced permeate concentrations below 600 ppm. This TDS range is generally associated with good palatability, according to the World Health Organization (WHO) [65]. Most evaluated membranes also satisfied the stricter WHO criterion of TDS below 300 ppm for excellent palatability [66]. Assuming that the observed proportional trend continues beyond the investigated range, the average permeate concentration of low-energy membranes is projected to exceed 600 ppm at feed concentrations surpassing approximately 12,200 ppm for a recovery of 0.8 and 9200 ppm for a recovery of 0.9. However, under the baseline 41 bar pressure limit, the maximum allowable pressure would be reached before the feed concentration attained these projected thresholds. Overall, HSBRO maintained good permeate quality under the investigated operating conditions, and the projected 600 ppm thresholds indicate the theoretical feed salinity range beyond which permeate quality may become a critical consideration in membrane selection.

Table 7
Predicted HSBRO performance at selected feed concentrations and recoveries under the baseline 41 bar and hypothetical 81 bar pressure limits.

P_{limit} (bar)	r	C_{feed} (ppm)	P_{peak} (bar)	SEC (kWh/m^3)	C_{perm} (ppm)
41	0.800	7150	36.08–40.99	0.728–0.926	64.1–651.1
41	0.900	3540	36.02–40.93	0.522–0.722	42.1–390.0
81	0.800	15,550	75.11–80.98	1.436–1.631	139.5–1292
81	0.900	7710	75.09–80.96	0.986–1.187	91.6–849.3
81	0.558	35,000	75.01–80.88	2.110–2.305	212.1–1962

Table 7 reports the minimum–maximum ranges of peak pressure, SEC, and average permeate concentration across the 26 membranes,

with the pressure criterion applied to the highest peak pressure among the membranes. The calculations used an aqueous NaCl feed at 25 °C, with the remaining parameters following Section 2.7 and Table 5. For the hypothetical 81 bar cases, the BWRO membranes were assumed to withstand the higher pressure while retaining their original transport parameters. Under the 41 bar limit, feed concentrations of 7150 and 3540 ppm were evaluated near the pressure limit at total recoveries of 0.8 and 0.9, respectively. Increasing the assumed pressure limit to 81 bar extended the corresponding feed concentrations to 15,550 and 7710 ppm. Their approximately twofold difference is consistent with the effect of recovery on maximum module osmotic pressure described in the discussion of Fig. 4. At a feed concentration of 35,000 ppm and a reduced recovery of 0.558, peak pressures ranged from 75.01 to 80.88 bar, with SEC values of 2.110–2.305 kWh/m^3. Although all 26 membranes satisfied the hypothetical pressure limit, their average permeate concentrations ranged from 212.1 to 1962 ppm, indicating substantial differences in permeate quality despite the relatively narrow SEC range. Thus, satisfying the pressure limit alone does not guarantee the required permeate quality. Extending the evaluated HSBRO configuration to higher salinities therefore requires coordinated selection of operating recovery, pressure capability, and membrane salt selectivity.

The effects of recovery and feed concentration on the TACC, TOC, and TAC of the HSBRO system using the 26 commercial RO membranes are shown in Fig. 5. Increasing the recovery from 0.8 to 0.9 increased the TACC, TOC and TAC by 7.47%, 12.08%, and 8.71%, respectively (Fig. 5a). Increasing the feed concentration from 1000 to 3000 ppm produced corresponding increases of 3.20%, 17.95%, and 6.82%, while a further increase to 5000 ppm elevated these costs by 3.10%, 15.22%, and 6.38%, respectively (Fig. 5b). These results demonstrate that TOC is more sensitive in relative terms to changes in recovery and feed concentration than TACC.

Tables 8 and 9 clarify the cost structure underlying the different sensitivities of TACC and TOC observed in Fig. 5. Pretreatment capital cost emerged as the largest individual component, accounting for approximately 54.6%–61.8% of the TAC, whereas electricity cost constituted approximately 9.7%–13.3%. The predominance of CAPEX is broadly consistent with previous assessments of high-salinity BWRO plants, where the total capital and electricity cost contributions were 45%–65% and 15%–30%, respectively [67]. The lower electricity contribution observed for HSBRO can be partially attributed to its relatively small treatment capacity and the dominant pretreatment capital cost, although differences in process boundaries and cost classification should also be considered. Because the major capital components were primarily determined by treatment capacity and system configuration, TACC varied only slightly among membrane types. Conversely, membrane properties affected the required operating pressure and SEC, which directly influenced the electricity consumption and yielded substantial variations in TOC. The maximum difference in TACC among the membrane types was approximately $20/yr, while the corresponding electricity cost difference reached approximately $76.8/yr. These findings indicate that the absolute cost level is governed by CAPEX, whereas the economic variation across membranes and operating conditions is governed by SEC and electricity cost, making membrane selection important for improving the relative economic performance of HSBRO within a specific process configuration.

To facilitate quantitative comparison across membranes and operating conditions, Tables S2 and S3 in the Supplementary Material summarize the SEC, average permeate concentration, and SWC obtained for all 26 membranes at the examined feed concentrations and recoveries. These data provide a performance matrix for assessing the range of HSBRO performance achievable using current commercial RO membranes.

3.2.2. *Effect of the switch-over timing between the semi-batch and batch phases*

The overall performance of HSBRO varies substantially with the phase-switching point, reflecting its flexible operation over the relative contributions of the semi-batch and batch phases. In both Figs. 6 and 7, panels (a), (b), and (c) present the variations in SEC, average permeate concentration, and SWC, respectively, in relation to the fraction of the total recovery achieved during the batch pressurization phase (r_b/r). Detailed information regarding the corresponding vessel volume ratios is provided in the Supplementary Material (Table S4). This ratio determines the phase-switching point and thus controls the relative durations of the two phases. Fig. 8 illustrates this relationship through the pressure profiles: a higher r_b/r shifts the transition to batch pressurization earlier in the cycle. Consequently, the resulting trends established in Figs. 6 and 7 clarify how this adjustment in phase allocation affects each performance metric and indicate how the operating strategy can be selected according to the target energy consumption, permeate quality, and economic performance.

Increasing the batch-phase contribution generally reduced SEC and

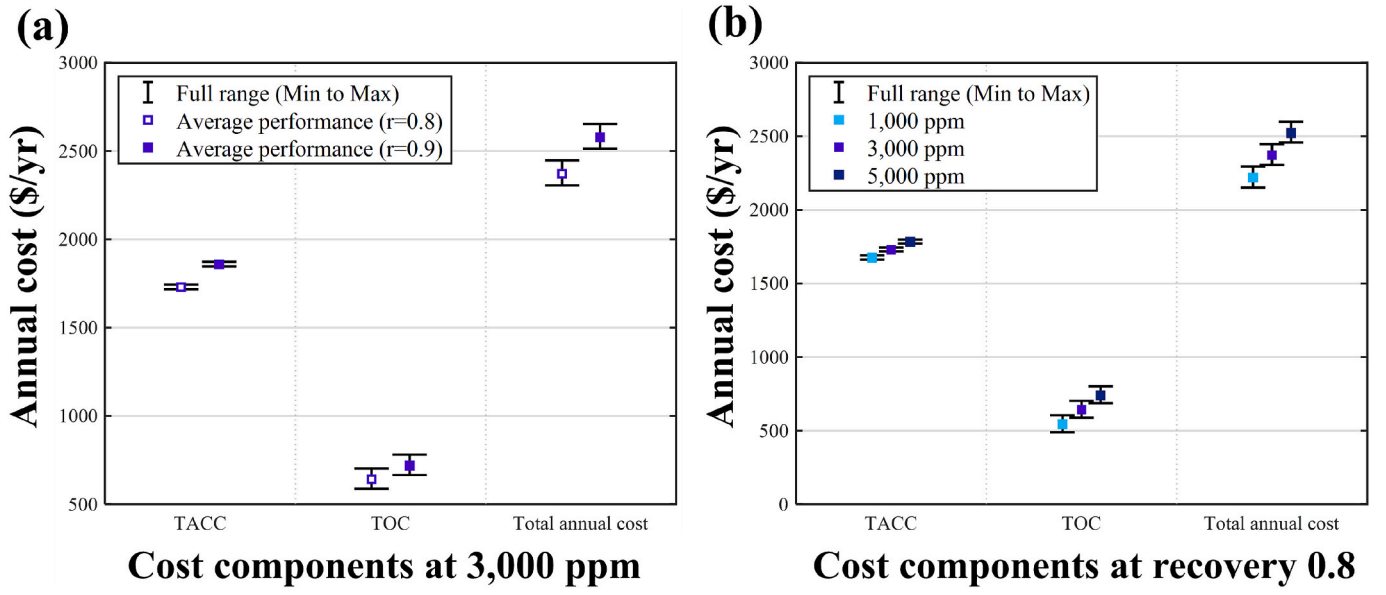


Fig. 5. Simulation results of annual cost component variations for the 26 commercial RO membranes within the HSBRO system under (a) different recovery ratios at a fixed feed concentration ($C_{feed} = 3000$ ppm) and (b) different feed concentrations at a fixed recovery ratio ($r = 0.8$).

Table 8
Cost breakdown of the HSBRO system by cost index for different membrane types at a feed concentration of 3000 ppm and a recovery ratio of 0.8.

Cost index		High-rejection type		Balanced type		Low-energy type	
		Value	Fraction	Value	Fraction	Value	Fraction
CAPEX	CC_{pre} ($)	11,636	59.33%	11,636	60.32%	11,636	61.83%
	CC_{HPP} ($)	954.59	4.87%	883.77	4.58%	791.98	4.21%
	CC_{recir} ($)	21.54	0.11%	24.41	0.13%	22.78	0.12%
	CC_{memb} ($)	900	4.59%	900	4.67%	900	4.78%
	CC_{WEV} ($)	615.8	3.14%	615.8	3.19%	615.8	3.27%
	TCC ($)	19,935	–	19,839	–	19,707	–
	TACC ($/yr)	1738.0	72.03%	1729.7	72.88%	1718.2	74.21%
OPEX ($/yr)	OC_{elec}	300.74	12.46%	269.93	11.37%	224.0	9.68%
	OC_{insure}	99.68	4.13%	99.20	4.18%	98.54	4.26%
	OC_{chem}	127.72	5.29%	127.72	5.38%	127.72	5.52%
	$OC_{replace}$	90	3.73%	90	3.79%	90	3.89%
	OC_{labor}	56.76	2.35%	56.76	2.39%	56.76	2.45%
	TOC	674.90	27.97%	643.62	27.12%	597.03	25.79%
TAC ($/yr)		2413		2373		2315	
SWC ($/m^3)		0.425		0.418		0.408	

Table 9
Cost breakdown of the HSBRO system by cost index for different membrane types at a feed concentration of 3000 ppm and a recovery ratio of 0.9.

Cost index		High-rejection type		Balanced type		Low-energy type	
		Value	Fraction	Value	Fraction	Value	Fraction
CAPEX	CC_{pre} ($)	11,636	54.64%	11,636	55.49%	11,636	56.76%
	CC_{HPP} ($)	1622.5	7.62%	1547.8	7.38%	1457.6	7.11%
	CC_{recir} ($)	21.54	0.10%	24.41	0.12%	22.78	0.11%
	CC_{memb} ($)	900	4.23%	900	4.29%	900	4.39%
	CC_{WEV} ($)	1000	4.70%	1000	4.77%	1000	4.88%
	TCC ($)	21,420	–	21,318	–	21,189	–
	TACC ($/yr)	1867.5	71.28%	1858.6	72.05%	1847.3	73.25%
OPEX ($/yr)	OC_{elec}	347.83	13.28%	316.99	12.29%	271.02	10.75%
	OC_{insure}	107.10	4.09%	106.59	4.13%	105.94	4.20%
	OC_{chem}	143.69	5.48%	143.69	5.57%	143.69	5.70%
	$OC_{replace}$	90	3.44%	90	3.49%	90	3.57%
	OC_{labor}	63.86	2.44%	63.86	2.48%	63.86	2.53%
	TOC	752.47	28.72%	721.13	27.95%	674.51	26.75%
TAC ($/yr)		2620		2580		2522	
SWC ($/m^3)		0.410		0.404		0.395	

average permeate concentration, while its effect on SWC depended on recovery. As described in Section 2.1, HSBRO has a lower average system concentration than semi-batch RO, although both processes reach a comparable final concentration at the target recovery. Fig. 8 reveals a clear energy benefit by showing that the applied-pressure trajectory of HSBRO remains below that of semi-batch RO throughout most of the operation. The lower average system concentration reduces the osmotic pressure difference and required operating pressure as described by Eq. (1), while the lower salt concentration at the membrane surface reduces salt flux according to Eq. (2). Thus, increasing the contribution of the batch phase reduces the duration of membrane exposure to highly concentrated solution, lowering both the average permeate concentration and SEC. However, increasing the batch-phase contribution inevitably requires a larger work-exchange vessel, increasing the system footprint and capital cost. A larger vessel also requires a higher recirculation flow rate during the purge-and-refill phase, increasing pressure losses and pumping energy. At a recovery of 0.8, the additional vessel cost outweighed the electricity cost savings, resulting in an increase in SWC. At a recovery of 0.9, the greater electricity cost savings initially lowered SWC. However, as vessel volume increased further, the additional energy savings became smaller while vessel costs continued to rise, causing SWC to reach a minimum and then increase.

A comparison of Figs. 6 and 7 demonstrates that the effect of phase allocation on HSBRO performance is considerably stronger at a total recovery of 0.9 than at 0.8. This greater response indicates that the selection of the phase-switching point becomes more consequential during high-recovery operations. Specifically, at a recovery ratio of 0.9, the SEC decreased by 37%, 39%, and 43% between the semi-batch and batch reference cases for the high-rejection, balanced, and low-energy membrane groups, respectively. These differences quantify the SEC reductions achieved by shifting the phase allocation from the semi-batch reference case to the batch reference case for each membrane group. When the work-exchange vessel volume was restricted to 50% of that required for pure batch RO, the corresponding SEC values were 0.613, 0.559, and 0.475 kWh/m^3. The captured SEC benefit quantifies the SEC reduction achieved by HSBRO relative to the SEC difference between the semi-batch and batch reference cases, as defined in Appendix E of the Supplementary Material. On this basis, the configuration captures approximately 99.8%–100.1% of the reference SEC reduction while substantially decreasing the required vessel volume.

The energy benefit associated with work-exchange vessel sizing is further quantified in Fig. 8. At a total recovery of 0.8, increasing the vessel volume ratio relative to that of pure batch RO increased from 0.3 to 0.5 and 0.7, the SEC reduction (ΔSEC) relative to that of pure semi-batch RO increased from 0.085 to 0.098 and 0.101 kWh/m^3, respectively. However, the additional SEC reduction decreased from 0.013 kWh/m^3 between the 0.3 and 0.5 cases to only 0.003 kWh/m^3 between the 0.5 and 0.7 cases. This result demonstrates diminishing returns as the system approaches the pure batch limit. A qualitatively similar relationship between cylinder size and energy performance was reported for improved CCRO [68]. At 95% recovery, a cylinder approximately 70% smaller than the baseline cylinder used in that study incurred an SEC penalty of no more than 2%. Both studies indicate that adjusting the contributions of the operating modes can reduce vessel

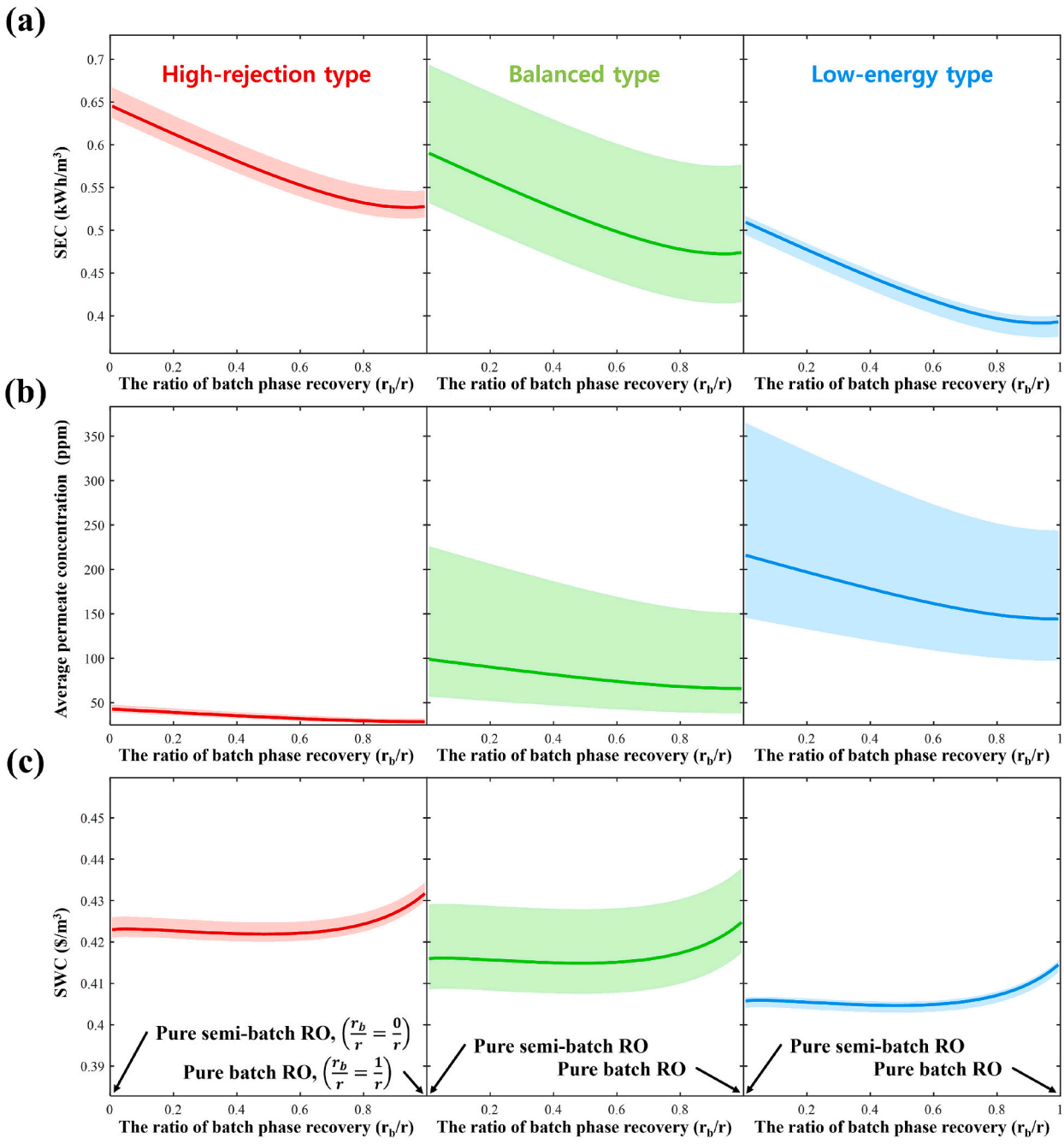


Fig. 6. Evaluation of HSBRO system performance as a function of the switching point between semi-batch and batch phases at an overall recovery of 0.8 and a feed concentration of 3000 ppm. The switching point is represented by the fraction of the overall recovery achieved during the batch phase, (r_b/r), where $r_b/r = 0$ and $r_b/r = 1$ correspond to pure semi-batch and batch RO states, respectively. (a) SEC, (b) average permeate concentration, and (c) SWC for each membrane type. The left (red), center (green), and right (blue) columns represent the high-rejection, balanced, and low-energy membranes, respectively. The solid lines indicate the mean performance of the RO membranes in each category, while the shaded regions represent the corresponding performance ranges across the RO membranes.

requirements while retaining substantial energy benefits. For HSBRO, the present results indicate that most of the energy, permeate quality, and economic benefits of batch RO can be retained with a substantially smaller work-exchange vessel. At the same time, the phase-switching point must be selected to exploit this operational flexibility while balancing performance gains against the associated penalties, including increased plant size, higher CAPEX, and additional purge-and-refill energy consumption.

3.3. *Case studies for effective utilization of the HSBRO system*

The preceding sections described the quantification of the achievable performance range of HSBRO using current commercial RO membranes and clarified the trade-off between energy consumption and permeate quality. Building on these results, this section examines RO membrane advancement and evaluates HSBRO in terms of carbon emissions and associated costs.

3.3.1. *Effects of RO membrane advancement*

To evaluate the potential effects of advances in RO membrane

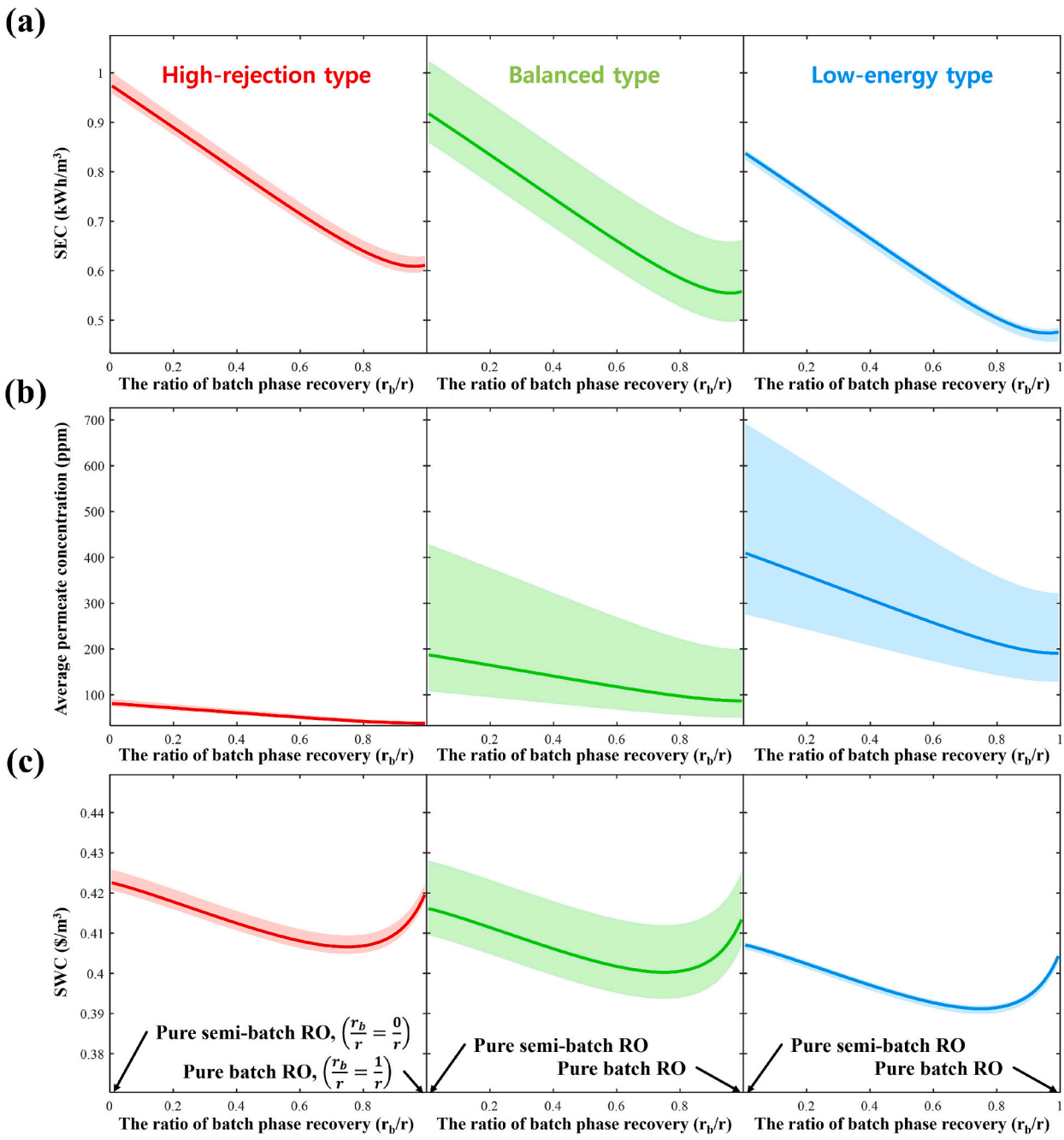


Fig. 7. Evaluation of HSBRO system performance as a function of the switching point between semi-batch and batch phases at an overall recovery of 0.9 and a feed concentration of 3000 ppm. The switching point is represented by the fraction of the overall recovery achieved during the batch phase, (r_b/r), where $r_b/r = 0$ and $r_b/r = 1$ correspond to pure semi-batch and batch RO states, respectively. (a) SEC, (b) average permeate concentration, and (c) SWC for each membrane type. The left (red), center (green), and right (blue) columns represent the high-rejection, balanced and low-energy membranes, respectively. The solid lines indicate the mean performance of the RO membranes in each category, while the shaded regions represent the corresponding performance ranges across the RO membranes.

technology, the SEC, SWC, and permeate concentration of HSBRO were calculated by progressively increasing the water permeability from 0.9×10^{-11} to 5.0×10^{-11} m/(s·Pa), as presented in Fig. 9. The recently reported SOTA membranes (Fig. 9c) exhibit water permeabilities of up to approximately 2.3×10^{-11} m/(s·Pa) [69–72], and this maximum value is marked as the SOTA level in the SEC and SWC plots presented in Fig. 9a and Fig. 9b, respectively. If membranes achieving this permeability level were to be commercialized and implemented in the HSBRO process, the SEC of low-energy membranes would decrease by 2.6% and 2.2% at recoveries of 0.8 and 0.9, respectively. The corresponding reductions for high-rejection membranes would reach 26.9% and 23.3%. The resulting SWC reductions would be only 0.3% for low-energy membranes at both recoveries, compared with 4.3% and 3.9% for high-rejection membranes at recoveries of 0.8 and 0.9, respectively. Although the magnitude of improvement differs depending on the initial membrane properties, the SEC and SWC curves flatten as A approaches the reported SOTA permeability level. This suggests that the benefits of increasing A already approach saturation in this range and that further improvements in water permeability exert only limited effects on SEC and SWC.

At higher A values within the investigated range, further increases in A yielded progressively smaller reductions in SEC and SWC. Therefore,

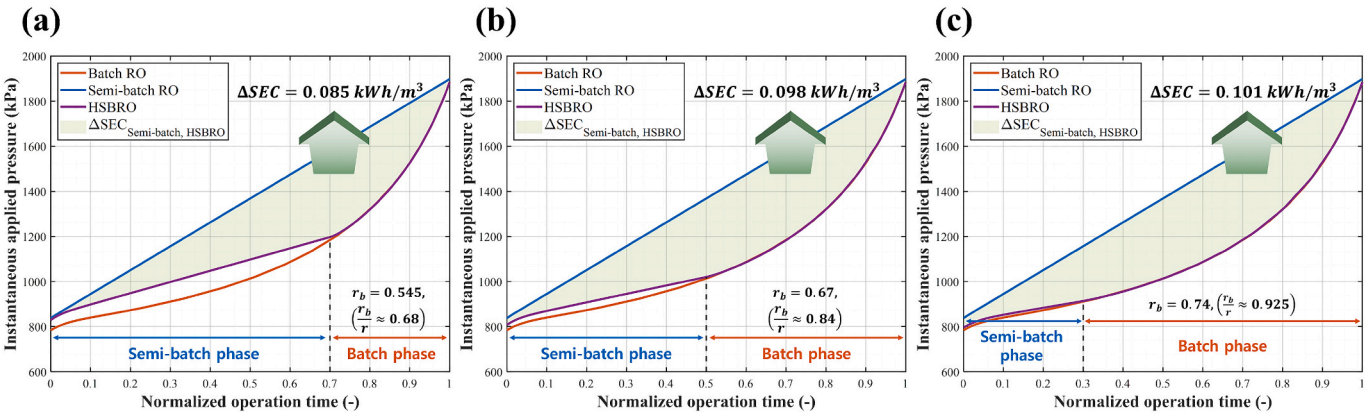


Fig. 8. Applied pressure profiles of pure batch RO, pure semi-batch RO, and HSBRO during operation at an overall recovery of 0.8 at a feed concentration of 3000 ppm. The data in (a), (b), and (c) were calculated using the r_b values that restrict the HSBRO work-exchange vessel volume to 0.3, 0.5 and 0.7 times the vessel volume required for pure batch RO, respectively. The red, blue, and purple lines represent the pressure profiles of pure batch RO, pure semi-batch RO, and HSBRO, respectively. The vertical dashed lines indicate the switching point from the semi-batch phase to the batch phase in HSBRO. The green shaded regions represent the differences in the pressure–time integrals between pure semi-batch RO and HSBRO, corresponding to SEC reductions.

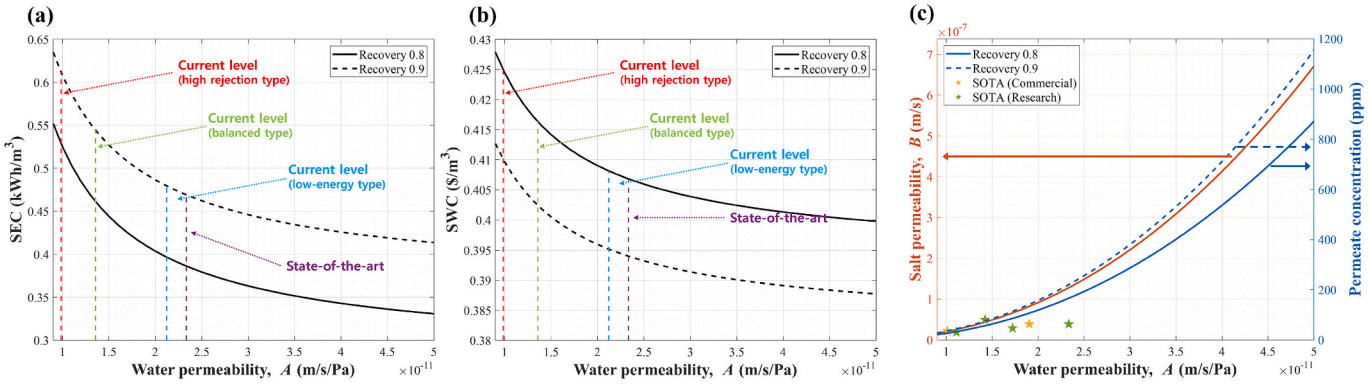


Fig. 9. Effect of advancements in RO membrane water permeability on HSBRO performance at a feed concentration of 3000 ppm. The water permeability was varied from 0.9×10^{-11} to 5.0×10^{-11} m/(s·Pa). (a) SEC and (b) SWC at recoveries of 0.8 (solid curves) and 0.9 (dashed curves). The colored vertical dashed lines indicate the current water permeability levels of the high-rejection, balanced, and low-energy membranes, while the purple dashed line indicates the maximum water permeability reported for SOTA membranes. (c) Salt permeability predicted from the fitted *A*–*B* relationship for current commercial RO membranes and the corresponding average permeate concentration at recoveries of 0.8 and 0.9. The yellow and green stars represent the reported properties of commercial and research-stage SOTA membranes, respectively.

the analysis shifted to the effect of increasing A on salt permeability and permeate quality. As shown in Fig. 9c, the fitted A–B relationship derived from current commercial RO membranes indicates that B and average permeate concentration increase with A. This quality penalty is more restrictive for low-energy membranes, which exceed the 600 ppm threshold after A increases by approximately 99% and 74% at recoveries of 0.8 and 0.9, respectively. Thus, when A and B remain coupled, further permeability enhancement is constrained by both limited energy and cost benefits and deterioration in permeate quality.

Based on the combined trends in Fig. 9, we propose $A = 2.5 \times 10^{-11}$ m/(s·Pa) as a condition-specific water permeability target for HSBRO. We identified this target for a feed concentration of 3000 ppm and total recoveries of 0.8 and 0.9, using the fitted A–B relationship and the process and economic assumptions specified in Section 2.7 and Table 5. Further increasing A beyond this target, up to the scenario endpoint of 5.0×10^{-11} m/(s·Pa), yielded additional SWC reductions below approximately 1.5% at both recoveries. Sensitivity analyses at an overall recovery of 0.8 showed that the diminishing-return trends in SEC and SWC persisted across feed concentrations of 1000–5000 ppm, whereas compliance with the 300 ppm palatability benchmark depended on feed salinity and the fitted A–B relationship (Appendix F, Supplementary Material). At 5000 ppm, the average permeate concentration at the proposed A exceeded this benchmark under the fitted relationship but remained below it under the high-selectivity relationship. Under the assumed A–B coupling, further increases in A beyond the target provide increasingly marginal performance benefits while increasing permeate concentration. These combined trends support retaining the proposed A target and prioritizing reductions in B at this A to extend its applicability to higher feed salinities while satisfying the selected permeate quality requirement.

As indicated by the star markers in Fig. 9c, current SOTA RO membrane studies have extended water permeability beyond the range of commercial low-energy membranes while maintaining high salt rejection. The material designs and fabrication or modification routes for these SOTA RO membranes are summarized in Table 10, covering nanostructured transport pathways and surface or posttreatment strategies. Continued advances in membrane materials, structural design, and scalable fabrication will be essential for translating these high-performance membranes into commercial RO products. Their implementation in HSBRO could reduce energy requirements while securing target permeate quality under high-recovery and high-salinity conditions, thereby expanding the feasible operating window toward minimal liquid discharge and zero liquid discharge (MLD/ZLD) applications.

Table 10
SOTA RO membrane strategies for improving water permeability while maintaining high salt rejection, highlighting fabrication and modification routes that can guide the development of scalable RO membranes.

Design concept/material	Fabrication or modification route	Improvement	Ref.
ZIF-8 nanosheets	ZIF-8 nanosheet incorporation via interfacial polymerization	37% higher *A* than the pristine membrane	[73]
Crown ether–LDH	*Co*-precipitation of 15CE-LDH, incorporation via interfacial polymerization	≥ 190% higher *A* than pristine TFC	[74]
Supramolecular subnanochannels	Interfacial supramolecular self-assembly of tetra-oligomers (PEG-mediated hydrogen bonding)	Water flux of 69.9 LMH at 15.5 bar; ≥ 99.6% NaCl rejection	[69]
Taurine surface modification	One-step covalent grafting of taurine onto a PA layer	≥ 40% higher flux with maintained NaCl rejection	[75]
Alkaline posttreated PA	NaOH hydrolysis posttreatment of PA RO membrane	2 – fold higher *A* with 98.5% NaCl rejection	[76]
Citric acid–Fenton modified PA	Citric acid-chelated Fenton oxidation posttreatment	Higher perm-selectivity, enhanced antifouling	[70]

Table 11
SCE ($kgCO_2$-eq/m^3) associated with HSBRO desalination for different power sources, membrane types, and recovery ratios at a feed concentration of 3000 ppm.

Components	$r = 0.8$			$r = 0.9$		
	High-rejection type	Balanced type	Low-energy type	High-rejection type	Balanced type	Low-energy type
PV panels	0.041	0.036	0.030	0.047	0.042	0.037
Wind turbines	0.023	0.020	0.017	0.026	0.023	0.020
Diesel fuel	0.469	0.410	0.349	0.543	0.483	0.422

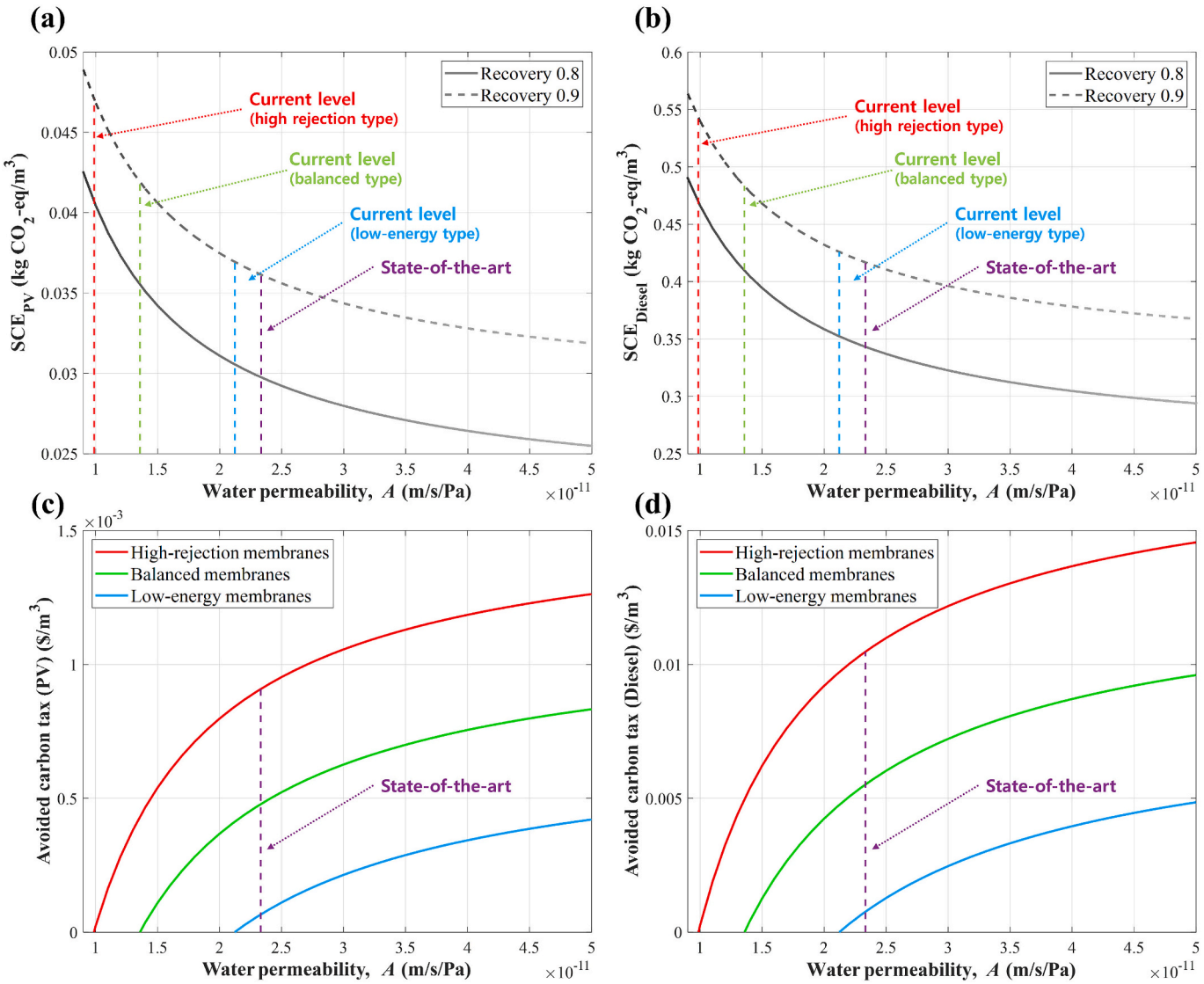


Fig. 10. Effect of advancements in RO membrane water permeability on SCE under (a) PV-powered and (b) diesel-powered electricity at recoveries of 0.8 and 0.9. Resulting avoided carbon tax equivalent costs under (c) PV-powered and (d) diesel-powered electricity at a recovery of 0.8 under a feed concentration of 3000 ppm.

3.3.2. Carbon emissions and associated costs under different electricity supply scenarios

The calculated SCE values for HSBRO are summarized in Table 11. The simulations were performed at a feed concentration of 3000 ppm and recoveries of 0.8 and 0.9 using the average properties of each membrane type. The absolute SCE was found to be governed primarily by the power source, following the order of diesel fuel, PV panels, and wind turbines. In each power source case, the low-energy membranes reduced the SCE by approximately 26% at a recovery of 0.8 and by 21–23% at a recovery of 0.9, relative to the high-rejection membranes. However, increasing the recovery from 0.8 to 0.9 raised SCE by 13%–16%, 15%–18%, and 18%–23% for the high-rejection, balanced, and low-energy membranes, respectively. Thus, the carbon benefit achieved through membrane selection can be partially offset by high-recovery operation. Accordingly, effective carbon management in HSBRO requires membrane type and recovery to be simultaneously considered.

The potential impacts of improved RO membrane water permeability on carbon emissions and carbon tax equivalent costs in HSBRO are presented in Fig. 10. PV power was selected as a practical low-carbon renewable source, whereas diesel-powered case was selected as a carbon-intensive fossil-based benchmark to establish the upper range of carbon emissions among the considered power sources. As shown in Fig. 10a and b, SCE decreased as A increased, consistent with the SEC trend shown in Fig. 9a. The corresponding reduction is presented in Fig. 10c and d as the avoided carbon tax equivalent cost relative to the current technology level of each membrane type. Considering that the avoided cost is identical at recoveries of 0.8 and 0.9, a single result is presented for each power source. Based on the preceding SEC and SWC analyses, $A = 2.5 \times 10^{-11}$ m/(s·Pa) was used as a reasonable advancement level. At this permeability, the low-energy membranes provided avoided costs of $\$1.1 \times 10^{-4}\,m^{-3}$ under PV-powered conditions and $\$1.3 \times 10^{-3}\,m^{-3}$ under diesel-powered conditions, corresponding to a reduction of approximately 4.4%. The corresponding avoided costs for the high-rejection membranes were $\$9.5 \times 10^{-4}\,m^{-3}$ and $\$1.1 \times 10^{-2}\,m^{-3}$, respectively, which represent a reduction of approximately 28%. Although the preceding SEC and SWC analyses suggest that further increases in A provide limited process level benefits beyond this permeability range, the carbon analysis demonstrates that the remaining SEC reduction can still be translated into reduced SCE and carbon tax equivalent cost. Therefore, the estimated reductions in SCE and carbon tax equivalent costs provide additional justification for advancing RO membrane water permeability, provided that the target permeate quality is maintained.

Figs. 11a–d show the effect of carbon pricing on the carbon-adjusted SWC of HSBRO under the baseline economic assumptions. The sensitivity of these cost estimates to electricity price, annual interest rate, and the annual membrane replacement coefficient at the reference carbon price is examined in Appendix J of the Supplementary Material (Fig. S8). Over the examined carbon price range of 0–0.3 USD/kgCO_2-eq, the adjusted SWC under PV-powered conditions increased from approximately 0.410 to 0.424 USD/m^3 for the high-rejection membranes and from 0.395 to 0.406 USD/m^3 for the low-energy membranes. Conversely, the corresponding values under diesel-powered conditions increased to 0.573 and 0.523 USD/m^3, respectively. Fig. 11c and d quantify the contribution of the additional carbon-related cost to the total adjusted SWC. At the current reference carbon price of approximately $0.08297/kg$CO_2$-eq, the additional carbon-related costs accounted for approximately 0.8%–1.0% of the original SWC under PV-powered conditions and 8.9%–11.0% under diesel-powered conditions, depending on the membrane type. Under the maximum carbon price scenario examined in this study, which was set at $0.3/kg$CO_2$-eq, the additional carbon-related costs increased to approximately 2.8%–3.4% and 32.3%–39.7%, respectively. In each power source case, the carbon-related cost contribution was largest for the high-rejection membranes and smallest for the low-energy membranes because of their different SEC and SCE levels. These results indicate that carbon pricing has a limited effect on HSBRO economics when low-carbon renewable electricity is used, thereby avoiding a major cost burden. In contrast, under a carbon-intensive power supply, the carbon-related cost can account for a substantial share of the total water cost and should be explicitly incorporated into the economic evaluation of HSBRO. In particular, the larger carbon-related cost under diesel supply increases the economic value of SEC reduction, strengthening the incentive to select low-energy membranes. These findings support a common membrane selection strategy for both PV and diesel scenarios: minimizing the carbon-adjusted SWC while satisfying the target permeate quality.

Fig. 11e and f further evaluate whether the SWC reduction obtained by increasing the recovery ratio from 0.8 to 0.9 is retained after the additional carbon tax equivalent cost is included. Positive values indicate that a recovery ratio of 0.9 remains more economical than a recovery ratio of 0.8 after accounting for carbon cost. Under PV-powered conditions, the ΔSWC_{carbon} advantage decreased only gradually, and $Price_{carbon,BE}$, the carbon price at which the economic advantage of a 0.9 recovery ratio over a 0.8 recovery ratio is completely offset and ΔSWC_{carbon} becomes zero, was estimated to be 2.04–2.33 USD/kgCO_2-eq. Under diesel-powered conditions, however, the break-even prices were 0.20, 0.19, and 0.18 USD/kgCO_2-eq for the high-rejection, balanced, and low-energy membranes, respectively. These thresholds lie within the investigated range, demonstrating that the economic benefit of higher recovery is conditional on carbon price under a carbon-intensive electricity supply. At the reference carbon price of 0.08297 USD/kgCO_2-eq, increasing recovery from 0.8 to 0.9 reduced SWC by approximately 0.00693–0.00879 USD/m^3 under diesel-powered conditions. Low-energy membranes reached break-even at a lower carbon price because increasing recovery provided a smaller initial cost saving, although their absolute carbon-adjusted SWC remained the lowest. Thus, recovery selection should consider both electricity carbon intensity and carbon price: higher recovery remained favorable throughout the examined range under PV power, but only below the respective break-even prices under diesel power.

4. Conclusion

This study quantitatively evaluated the achievable performance range of HSBRO using current commercial RO membrane technology. The properties of 26 commercial RO membranes were incorporated into a nonideal HSBRO model to assess the SEC, permeate concentration, SWC, SCE, and carbon tax equivalent cost under different feed salinity and recovery conditions.

- At a representative feed concentration of 3000 ppm and a recovery ratio of 0.8, the commercial RO membranes had an SEC range of approximately 0.38–0.58 kWh/m^3, a permeate concentration range of 27–249 ppm, and an SWC range of approximately 0.406–0.431 USD/m^3. The membrane groups occupied distinct regions within this performance window.
- The achievable performance window shifted with feed salinity and recovery. At a recovery of 0.8, increasing the feed concentration from 1000 to 5000 ppm shifted the SEC range from approximately 0.21–0.41 to 0.55–0.75 kWh/m^3. Additionally, increasing the recovery from 0.8 to 0.9 increased the SEC by approximately 15.7%–21.1%, depending on the membrane type. Thus, membrane selection for severe HSBRO operation should be based on the operating window that satisfies the target permeate quality requirement rather than on SEC minimization alone.
- The RO membrane advancement analysis identified ($A = 2.5 \times 10^{-11}$ m/(s·Pa)) as a technically reasonable permeability level because further increases in A produced diminishing improvements in system performance. Future RO membrane development should aim to increase water permeability while preserving salt rejection in high-rejection membranes and to improve salt rejection

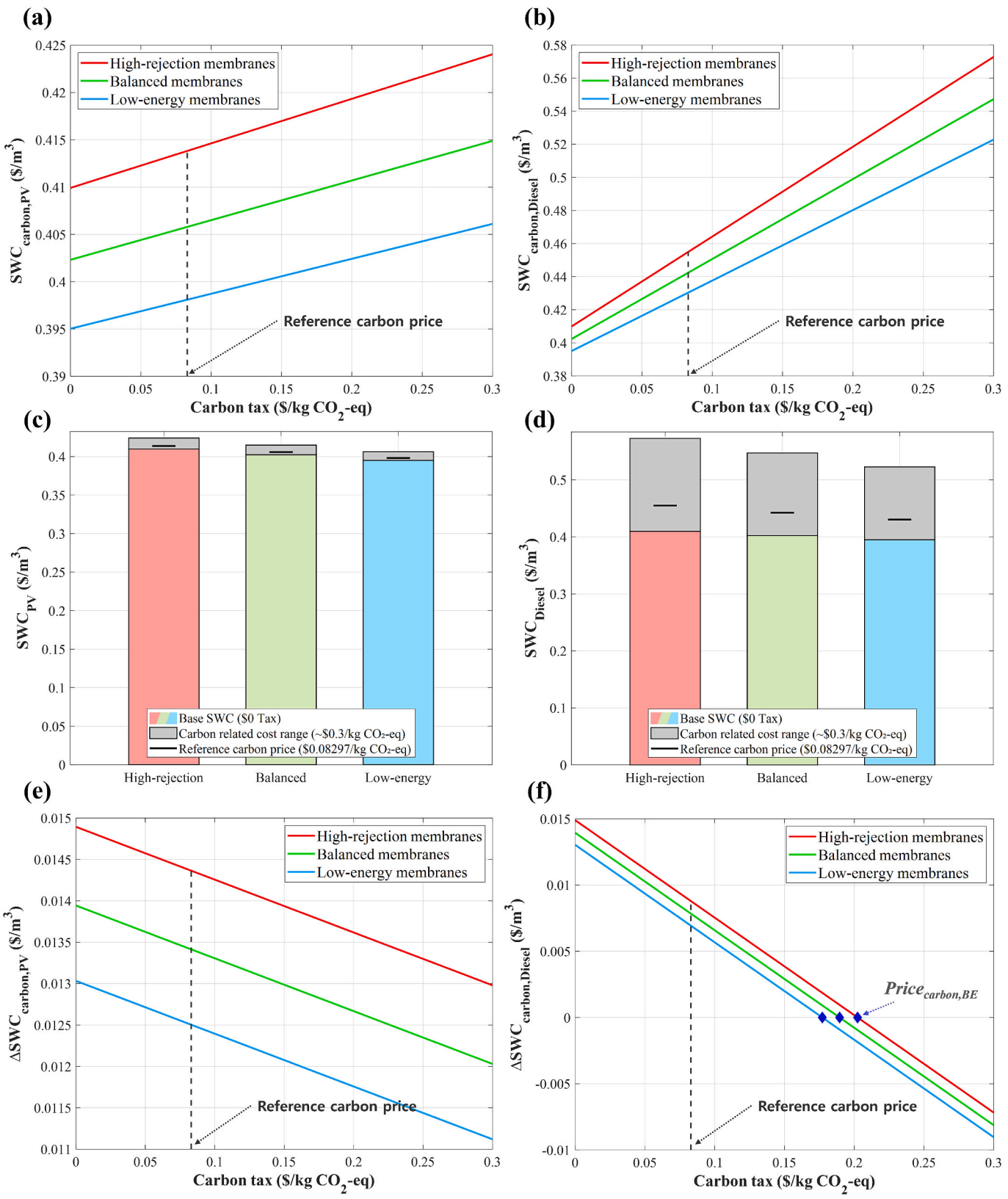


Fig. 11. Effect of carbon pricing on the carbon-adjusted SWC and net carbon-adjusted SWC advantage of high-recovery operation in the HSBRO system. Carbon-adjusted SWC as a function of carbon price under (a) PV-powered and (b) diesel-powered conditions. Contributions of the base SWC and additional carbon-related cost over the examined carbon price range under (c) PV-powered and (d) diesel-powered conditions. Here, the horizontal markers indicate the adjusted SWC at the reference carbon price. Net carbon-adjusted SWC advantage of increasing the recovery ratio from 0.8 to 0.9 under (e) PV-powered and (f) diesel-powered conditions. The positive values in (e) and (f) indicate that a recovery ratio of 0.9 remains economically favorable. The data presented in (a)–(d) were evaluated at a feed concentration of 3000 ppm and a recovery of 0.9.

while retaining the existing permeability advantage of low-energy membranes.

- As the carbon price increased from 0 to 0.3 USD/kgCO_2-eq, the additional carbon-related cost accounted for approximately 2.8%–3.4% of the original SWC under PV-powered conditions and 32.3%–39.7% under diesel-powered conditions. The $Price_{carbon,BE}$ for offsetting the economic advantage of a 0.9 recovery ratio over a 0.8 recovery ratio was 2.04–2.33 USD/kgCO_2-eq for PV-powered operation and 0.18–0.20 USD/kgCO_2-eq for diesel-powered operation. These results indicate that although carbon pricing exerts a limited economic influence under low-carbon renewable electricity, it can become a substantial cost burden under a carbon-intensive power supply. Nevertheless, high-recovery operation remains economically favorable across most of the examined carbon price range.

The assumptions of an NaCl feed and adequately controlled fouling and scaling limit the applicability of the results to real brackish waters and long-term operation. The proposed permeability target depends on the operating conditions and the assumed *A*–*B* relationship. The carbon analysis focused on emissions associated with electricity supply and did not assess broader environmental impacts. Within this scope, this study establishes a robust thermodynamic and techno-economic baseline that bridges the gap between intrinsic membrane properties and macro-level sustainability of HSBRO system. By defining practical permeability targets and quantifying the cost implications of carbon pricing, the integrated framework presented herein provides essential guidelines for the design, optimization, and deployment of next-generation HSBRO systems in a carbon-constrained era.

Declaration of competing interest

The authors declare that they have no known competing financial interests or personal relationships that could have appeared to influence the work reported in this paper.

Acknowledgements

This study was supported by the National Research Foundation of Korea (NRF) grant funded by the Korea government (MSIT) (RS-2024-00355308).

Appendix A. Supplementary data

Supplementary data to this article can be found online at https://doi.org/10.1016/j.desal.2026.120952.

Data availability

Data will be made available on request.

References

[1] A.F. Velani, V.S. Narwane, B.B. Gardas, Contribution of internet of things in water supply chain management: a bibliometric and content analysis, J. Model. Manag. 18 (2022) 549–577.
[2] M.T. Al-Nory, A. Brodsky, B. Bozkaya, S.C. Graves, Desalination supply chain decision analysis and optimization, Desalination 347 (2014) 144–157.
[3] A.M. Fathollahi-Fard, A. Ahmadi, S.M. Al-e-Hashem, Sustainable closed-loop supply chain network for an integrated water supply and wastewater collection system under uncertainty, J. Environ. Manag. 275 (2020) 111277.
[4] F. Tahir, S.G. Al-Ghamdi, T. Al-Ansari, Climate change risks and resilience strategies for desalination plants in the Gulf region, Renew. Sust. Energ. Rev. 227 (2026) 116488.
[5] UN-Water, World Water Assessment Programme, the United Nations World Water Development Report 2024: Water for Prosperity and Peace, Paris, 2024.
[6] J.A. Carballo, J. Bonilla, L. Roca, A. De la Calle, P. Palenzuela, D.C. Alarcón-Padilla, Optimal operating conditions analysis for a multi-effect distillation plant according to energetic and exergetic criteria, Desalination 435 (2018) 70–76.
[7] M. Al-Hamahmy, H.E. Fath, K. Khanafer, Techno-economical simulation and study of a novel MSF desalination process, Desalination 386 (2016) 1–12.
[8] N. Ghaffour, T.M. Missimer, G.L. Amy, Technical review and evaluation of the economics of water desalination: current and future challenges for better water supply sustainability, Desalination 309 (2013) 197–207.
[9] M. Elimelech, W.A. Phillip, The future of seawater desalination: energy, technology, and the environment, Science 333 (2011) 712–717.
[10] E. Jones, M. Qadir, M.T. van Vliet, V. Smakhtin, S.-m. Kang, The state of desalination and brine production: a global outlook, Sci. Total Environ. 657 (2019) 1343–1356.
[11] J. Kim, K. Park, D.R. Yang, S. Hong, A comprehensive review of energy consumption of seawater reverse osmosis desalination plants, Appl. Energy 254 (2019) 113652.
[12] D.M. Warsinger, E.W. Tow, K.G. Nayar, L.A. Maswadeh, J.H. Lienhard V, Energy efficiency of batch and semi-batch (CCRO) reverse osmosis desalination, Water Res. 106 (2016) 272–282.
[13] M. Li, Y. Heng, J. Luo, Batch reverse osmosis: a new research direction in water desalination, Sci. Bull. 65 (2020) 1705–1708.
[14] K. Park, P.A. Davies, A compact hybrid batch/semi-batch reverse osmosis (HBSRO) system for high-recovery, low-energy desalination, Desalination 504 (2021) 114976.
[15] E. Hosseinipour, S. Karimi, S. Barbe, K. Park, P.A. Davies, Hybrid semi-batch/batch reverse osmosis (HSBRO) for use in zero liquid discharge (ZLD) applications, Desalination 544 (2022) 116126.
[16] H.S. Kim, J. Byun, A. Jeong, G. Kim, J. Lee, T.-m. Hwang, Y.-G. Park, K. Park, Sustainable operation of hybrid semi-batch/batch reverse osmosis by additional purge-and-refill phase: optimization and life cycle assessment, Desalination 616 (2025) 119364.
[17] J.R. Werber, C.O. Osuji, M. Elimelech, Materials for next-generation desalination and water purification membranes, Nat. Rev. Mater. 1 (2016) 16018.
[18] D.M. Davenport, A. Deshmukh, J.R. Werber, M. Elimelech, High-pressure reverse osmosis for energy-efficient hypersaline brine desalination: current status, design considerations, and research needs, Environ. Sci. Technol. Lett. 5 (2018) 467–475.
[19] G. Pearce, Introduction to membranes: membrane selection, Filtr. Sep. 44 (2007) 35–37.
[20] M. Qasim, M. Badrelzaman, N.N. Darwish, N.A. Darwish, N. Hilal, Reverse osmosis desalination: a state-of-the-art review, Desalination 459 (2019) 59–104.
[21] A. Rani, S.W. Snyder, H. Kim, Z. Lei, S.-Y. Pan, Pathways to a net-zero-carbon water sector through energy-extracting wastewater technologies, npj clean Water 5 (2022) 49.
[22] L. Li, X. Wang, J. Miao, A. Abulimiti, X. Jing, N. Ren, Carbon neutrality of wastewater treatment - a systematic concept beyond the plant boundary, Environ. Sci. Ecotechnol. 11 (2022) 100180.
[23] G.M. Geise, H.B. Park, A.C. Sagle, B.D. Freeman, J.E. McGrath, Water permeability and water/salt selectivity tradeoff in polymers for desalination, J. Membr. Sci. 369 (2011) 130–138.
[24] T. Qiu, P. Davies, Concentration polarization model of spiral-wound membrane modules with application to batch-mode RO desalination of brackish water, Desalination 368 (2015) 36–47.
[25] Y.-Y. Lu, Y.-D. Hu, X.-L. Zhang, L.-Y. Wu, Q.-Z. Liu, Optimum design of reverse osmosis system under different feed concentration and product specification, J. Membr. Sci. 287 (2007) 219–229.
[26] K. Park, Y.H. Jang, J.W. Chang, D.R. Yang, Membrane transport behavior characterization method with constant water flux in pressure-assisted forward osmosis, Desalination 498 (2021) 114738.
[27] Y. Song, J. Moon, K. Park, Explainable AI for permeate flux prediction in forward osmosis: SHAP interpretability and theoretical validation for enhanced predictive reliability, Desalination 601 (2025) 118551.
[28] S. Chebil, A. Ruiz-García, S. Farhat, M. Bali, Long-term performance evaluation and fouling characterization of a full-scale brackish water reverse osmosis desalination plant, Water 16 (2024) 1892.
[29] V. Gekas, B. Hallström, Mass transfer in the membrane concentration polarization layer under turbulent cross flow: I. Critical literature review and adaptation of existing Sherwood correlations to membrane operations, J. Membr. Sci. 30 (1987) 153–170.
[30] K. Park, L. Burlace, N. Dhakal, A. Mudgal, N.A. Stewart, P.A. Davies, Design, modelling and optimisation of a batch reverse osmosis (RO) desalination system using a free piston for brackish water treatment, Desalination 494 (2020) 114625.
[31] G. Kim, K. Park, Application of batch reverse osmosis as an appropriate technology for inland desalination: design, modeling, and operating strategies, Desalination 592 (2024) 118185.
[32] J. Kim, S. Hong, A novel single-pass reverse osmosis configuration for high-purity water production and low energy consumption in seawater desalination, Desalination 429 (2018) 142–154.
[33] G. Schock, A. Miquel, Mass transfer and pressure loss in spiral wound modules, Desalination 64 (1987) 339–352.
[34] C.P. Koutsou, S.G. Yiantsios, A.J. Karabelas, A numerical and experimental study of mass transfer in spacer-filled channels: effects of spacer geometrical characteristics and Schmidt number, J. Membr. Sci. 326 (2009) 234–251.
[35] Y. Kim, J. Byun, K. Park, Y.-G. Park, Comprehensive analysis of energy saving and high-quality permeate production strategies for a large-scale seawater reverse osmosis desalination plant with diverse process configurations and external resource utilization, Desalination 596 (2025) 118292.
[36] A. Haidari, S. Heijman, W. Van der Meer, Visualization of hydraulic conditions inside the feed channel of reverse osmosis: a practical comparison of velocity between empty and spacer-filled channel, Water Res. 106 (2016) 232–241.

[37] K. Park, D.Y. Kim, D.R. Yang, Cost-based feasibility study and sensitivity analysis of a new draw solution assisted reverse osmosis (DSARO) process for seawater desalination, Desalination 422 (2017) 182–193.
[38] T.V. Bartholomew, N.S. Siefert, M.S. Mauter, Cost optimization of osmotically assisted reverse osmosis, Environ. Sci. Technol. 52 (2018) 11813–11821.
[39] K. Park, D.Y. Kim, Y.H. Jang, M.-g. Kim, D.R. Yang, S. Hong, Comprehensive analysis of a hybrid FO/crystallization/RO process for improving its economic feasibility to seawater desalination, Water Res. 171 (2020) 115426.
[40] J. Lim, J. Park, K. Park, J. Kim, Design of hybrid desalination process using waste heat and cold energy from LNG power plant increasing energy and economic potential, J. Clean. Prod. 452 (2024) 141998.
[41] D. Patel, A. Mudgal, V. Patel, J. Patel, K. Park, P. Davies, R.R. Alegre, Energy, exergy, economic and environment analysis of standalone forward osmosis (FO) system for domestic wastewater treatment, Desalination 567 (2023) 116995.
[42] D. Ankoliya, A. Mudgal, M.K. Sinha, P. Davies, K. Park, R.R. Alegre, V. Patel, J. Patel, Techno-economic analysis of integrated bipolar membrane electrodialysis and batch reverse osmosis for water and chemical recovery from dairy wastewater, J. Clean. Prod. 420 (2023) 138264.
[43] Z. Zhang, A. Atia, J. Andrés-Mañas, G. Zaragoza, V. Fthenakis, Comparative techno-economic assessment of osmotically-assisted reverse osmosis and batch-operated vacuum-air-gap membrane distillation for high-salinity water desalination, Desalination 532 (2022) 115737.
[44] J. Moon, D.Y. Kim, J.H. Kim, K. Park, Cost-based optimization, feasibility study, and sensitivity analysis of forward osmosis/crystallization/reverse osmosis with high-temperature operation for high-salinity seawater desalination, Desalination 580 (2024) 117531.
[45] W.D. Seider, D.R. Lewin, J. Seader, S. Widagdo, R. Gani, K.M. Ng, Product and Process Design Principles: Synthesis, Analysis and Evaluation, John Wiley & Sons, 2016.
[46] R. Turton, R.C. Bailie, W.B. Whiting, J.A. Shaeiwitz, D. Bhattacharyya, Analysis, Synthesis and Design of Chemical Processes, Prentice Hall, 2012.
[47] N. Sawaki, C.-L. Chen, Cost evaluation for a two-staged reverse osmosis and pressure retarded osmosis desalination process, Desalination 497 (2021) 114767.
[48] A. Nafey, M. Sharaf, L. García-Rodríguez, Thermo-economic analysis of a combined solar organic rankine cycle-reverse osmosis desalination process with different energy recovery configurations, Desalination 261 (2010) 138–147.
[49] O.G. Kaoud, Q.N. Al-Oweiti, M.H. Elbassoussi, S. Rehman, S.M. Zubair, Battery versus hydrogen storage for renewable-powered RO desalination: a technoeconomic and environmental analysis in coastal Saudi Arabia, Int. J. Hydrog. Energy 197 (2026) 152466.
[50] International Carbon Action Partnership, EU Emissions Trading System (EU ETS). https://icapcarbonaction.com/en/ets/eu-emissions-trading-system-eu-ets, 2025 (accessed 16 July 2026).
[51] U.K. Kesieme, N. Milne, H. Aral, C.Y. Cheng, M. Duke, Economic analysis of desalination technologies in the context of carbon pricing, and opportunities for membrane distillation, Desalination 323 (2013) 66–74.
[52] T. Qiu, P.A. Davies, Longitudinal dispersion in spiral wound RO modules and its effect on the performance of batch mode RO operations, Desalination 288 (2012) 1–7.
[53] R.V. Linares, Z. Li, V. Yangali-Quintanilla, N. Ghaffour, G. Amy, T. Leiknes, J. S. Vrouwenvelder, Life cycle cost of a hybrid forward osmosis – low pressure reverse osmosis system for seawater desalination and wastewater recovery, Water Res. 88 (2016) 225–234.
[54] C. Park, P.-K. Park, P.P. Mane, H. Hyung, V. Gandhi, S.-H. Kim, J.-H. Kim, Stochastic cost estimation approach for full-scale reverse osmosis desalination plants, J. Membr. Sci. 364 (2010) 52–64.
[55] H.B. Park, J. Kamcev, L.M. Robeson, M. Elimelech, B.D. Freeman, Maximizing the right stuff: the trade-off between membrane permeability and selectivity, Science 356 (2017) eaab0530.
[56] Z.M. Binger, M. Li, A. Dudchenko, De-risking high-recovery brackish water desalination via flow reversal and feed flushing using techno-economic assessment, Desalination 616 (2025) 119330.
[57] S.K. Patel, B. Lee, P. Westerhoff, M. Elimelech, The potential of electrodialysis as a cost-effective alternative to reverse osmosis for brackish water desalination, Water Res. 250 (2024) 121009.
[58] J.P. MacHarg, Energy optimization of brackish groundwater reverse osmosis desalination, , Contract No. 0804830845,, Texas Water Development Board, 2011.
[59] D. Patel, D. Ankoliya, M. Raninga, A. Mudgal, V. Patel, J. Patel, V. Mudgal, H. Choksi, Batch reverse osmosis: Evolution from the concept to the technology, in: A. Mudgal, P. Davies, M. Kennedy, G. Zaragoza, K. Park (Eds.), Advances in Water Treatment and Management. ICAWTM 2023, Springer, Singapore, 2024, pp. 175–200. Lecture Notes in Civil Engineering.
[60] A. Efraty, Closed circuit desalination series no-4: high recovery low energy desalination of brackish water by a new single stage method without any loss of brine energy, Desalin. Water Treat. 42 (2012) 262–268.
[61] T. Lee, Enhancement of Operational Flexibility in Reverse Osmosis Membrane Processes by Concentrate Recycling, , Dissertation,, University of California, Los Angeles, 2019.
[62] R.L. Stover, CCD starts a new generation for RO, Desalin. Water Reuse 6 (2011) 34–35.
[63] M. Ansari, M.A. Al-Obaidi, Z. Hadadian, M. Moradi, A. Haghighi, I.M. Mujtaba, Performance evaluation of a brackish water reverse osmosis pilot-plant desalination process under different operating conditions: experimental study, Cleaner Eng. Technol. 4 (2021) 100134.
[64] M. Alghoul, P. Poovanaesvaran, M. Mohammed, A. Fadhil, A. Muftah, M. Alkilani, K. Sopian, Design and experimental performance of brackish water reverse osmosis desalination unit powered by 2 kW photovoltaic system, Renew. Energy 93 (2016) 101–114.
[65] World Health Organization (Ed.), Guidelines for Drinking-Water Quality, fourth ed., World Health Organization, Geneva, 2011.
[66] World Health Organization, Total Dissolved Solids in Drinking-Water, World Health Organization, Geneva, 2003, p. 8.
[67] N. Voutchkov, Desalination Project Cost Estimating and Management, CRC press, 2018.
[68] M. Li, Effect of cylinder sizing on performance of improved closed-circuit RO (CCRO), Desalination 561 (2023) 116688.
[69] G. Lu, W. Shang, X. Ma, H. Xu, H. A, J. Sun, X. Li, M. Jia, S. Lu, J. Wu, X. Chen, S. Chen, J. Fan, A.K. An, Supramolecular nanocrystalline membranes with well-aligned subnanochannels for enhanced reverse osmosis desalination, Nat. Commun. 16 (2025) 6289.
[70] Z. Hong, X. Chen, Z. Wang, S. Yu, H. Lu, D. Wu, C. Gao, Enhanced anti-fouling and perm-selectivity properties of polyamide reverse osmosis membranes via citric acid-chelated Fenton oxidation modification, J. Membr. Sci. 734 (2025) 124476.
[71] LG Water Solutions, NanoH2O BWRO-ES-G2, 2026.
[72] Toray Industries, Inc., TorayRO_TLF-400ULD, 2025.
[73] H. You, X. Xu, W. Luo, L. Long, J. Du, S. Yi, W. Liu, Lamellar ZIF-8 nanosheets empowered thin-film nanocomposite membrane with synergistic sieving and rapid water transport for enhanced desalination, J. Membr. Sci. 745 (2026) 125261.
[74] C.-M. Chang, S. Zhu, F. Feng, Q. Zhao, S.B. Chen, 15-crown-5 functionalized layered double hydroxide enabling thin-film nanocomposite membranes for enhanced reverse osmosis desalination and boron removal, J. Membr. Sci. 736 (2025) 124732.
[75] B. Liu, F. Zhang, Z. Wang, T. Zhang, X. Zhou, Y. Chen, H. Sun, One-step surface modification of small molecule taurine for the preparation of high-performance reverse osmosis membranes, Colloids Surf. A Physicochem. Eng. Asp. 711 (2025) 136314.
[76] Y. Li, R. Wang, Z. Liu, Y. Zhao, L. Li, Q. Cao, F. Shao, Tailoring pore size and surface charge of polyamide reverse osmosis membranes via alkaline post-treatment for brackish water desalination, Polymers 18 (2026) 995.